Received 25 June 2023; revised 26 September 2023; accepted 25 October 2023. Date of publication 8 November 2023;
date of current version 19 December 2023. Recommended by Senior Editor Prof. Wei Zhang.

Digital Object Identifier 10.1109/OJCSYS.2023.3331193

On the Ratio of Reactive to Active Power in Wave Energy Converter Control

HAFIZ AHSAN SAID [1] (Student Member, IEEE), DEMIÁN GARCÍA-VIOLINI [1,2,3], NICOLÁS FAEDO [4], AND JOHN V. RINGWOOD [1] (Senior Member, IEEE)

[1]Centre for Ocean Energy Research (COER), Departement of Electronic Engineering, Maynooth University, W23 F2H6 Maynooth, Ireland
[2]Departamento de Ciencia y Tecnología, Universidad Nacional de Quilmes, Bernal B1876, Argentina
[3]Consejo Nacional de Investigaciones Científicas y Técnicas (CONICET) B1876, Argentina
[4]Marine Offshore Renewable Energy Lab., Department of Mechanical and Aerospace Engineering, Politecnico di Torino, 10138 Torino, Italy

CORRESPONDING AUTHOR: HAFIZ AHSAN SAID (e-mail: Hafiz.AhsanSaid@mu.ie)

This work was supported by MaREI, the Science Foundation Ireland (SFI) Research Centre for Energy, Climate and Marine, under Grant 12/RC/2302_P2. The work of Nicolás Faedo was supported by the European Union's Horizon 2020 Research and Innovation Programme, under the Marie Sklodowska-Curie Grant 101024372.

ABSTRACT Optimal control of wave energy converters (WECs), while converting wave energy into a usable form, such as electricity, may *inject* (reactive) power into the system at various points in the wave cycle. Though somewhat counter-intuitive, this action usually results in improved overall energy conversion. However, recent experimental results show that, on occasion, reactive power peaks can be significantly in excess of active power levels, leaving device developers with difficult decision in how to rate the power take-off of the system i.e. whether to cater for these high reactive power peaks, or limit power flow to rated (active) levels. The origins of these excessive power peaks are currently poorly understood, creating significant uncertainty in how to deal with them. In this paper, we show that, using both theoretical results and an illustrative simulation case study, *under matched controller conditions* (impedance-matching optimal condition), for both monochromatic and panchromatic sea-states, that the maximum peak reactive/active power ratio *never exceeds unity*. However, under mismatched WEC/controller conditions, this peak power ratio can exceed unity, bringing unrealistic demands on the power take-off (PTO) rating. The paper examines the various origins of system/controller mismatch, including modelling error, controller synthesis inaccuracies, and non-ideal PTO behaviour, highlighting the consequences of such errors on reactive power flow levels. This important result points to the need for accurate WEC modeling, while also showing the folly of catering for excessive reactive power peaks.

INDEX TERMS Optimal control, peak power ratio, reactive power, WEC control, wave energy.

I. INTRODUCTION

Wave energy converters (WECs) are devices used to harvest energy from ocean waves. Many WECs have been developed over the years to tap into this vast energy resource [1]. However, wave energy is not yet mature enough to compete with other renewable energy resources, such as wind or solar, due to its higher levelised cost of energy (LCoE) [2], [3]. In this regard, WEC control is considered an essential driver for economic performance of WEC technology [4]. WEC control aims to maximise energy absorption from waves, through active manipulation of the WEC motion at run-time, fully utilising the available capital infrastructure, to improve energy capture and, consequently, to reduce the resulting economic cost of wave energy [5]. In addition to the wide variety of existing WEC technologies, a large number of wave energy control systems are also reported in the literature, with a number implemented on prototype devices, ranging from relatively simple structures [6] (in essence based on fixed-parameter complex-conjugate control scheme) to on-line numerical optimisation-based controllers [7].

Optimal WEC control has been shown to require occasional reverse (*mechanical reactive*) power flow [4] from the grid-side. However, in the optimal WEC control sense, it is important to mention that 'reactive power' is different from

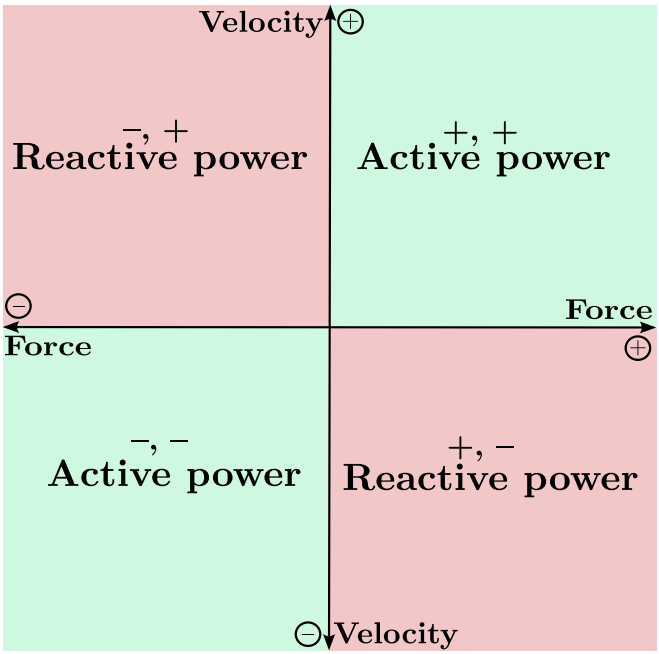

FIGURE 1. Active, and reactive, power flow regions for a wave energy converter under optimal control.

reactive power as defined for electrical power networks[1] where reactive power results from a phase difference between voltage and current. Rather, in the WEC case, reactive power is characterised by *a sign difference* between force and velocity (in mechanical power terms) or voltage and current (in electrical power terms). This is illustrated in Fig. 1. In the context of WECs, the 'force' and 'velocity' refer to the PTO (control) force and WEC velocity, denoted by $f_u(t)$ and $v(t)$ in Fig. 5, since the absorbed mechanical power is the product of the PTO (control) force and WEC velocity, i.e., $P_{abs} = v(t)f_u(t)$.

Fig. 2 presents a typical instantaneous power flow profile for an optimally controlled WEC, with green and red shaded areas representing active (forward) and reactive (reverse) power flow regions, respectively. However, not all WEC control algorithms utilise reactive power flow, which needs the entire wave-to-wire power train to be bi-directional. For example, a (suboptimal) passive WEC damping controller is common in some systems [9], which does not require reactive power, but its power absorption capability is significantly lower than that of a reactive WEC controller [8]. Hence, reactive WEC controllers, with a small cost overhead (relative to the main WEC structure and power take-off (PTO)) compared to passive WEC controllers, are essential to maximise power absorption from the available capital WEC infrastructure, leading to better overall economic performance.

[1]The interested reader is referred to [8] for a complete description of the differences between mechanical reactive power and reactive power in electrical networks.

The WEC PTO system must therefore handle both active and reactive power peaks and facilitate bi-directional power flow for a reactively controlled wave energy conversion system. However, to achieve a cost-effective design, it is imperative to accurately assess the active/reactive peak power needs of a reactively controlled WEC system to correctly rate the PTO system to maximise economic value, balancing energy capture capability with capital cost, with capacity factor a key parameter [8], [10]. Therefore, when reactive power peaks exceed the active power peaks, i.e., the reactive-to-active peak power ratio exceeds unity, there are significant cost implications for PTO system capacity, as the excessive reactive power peaks may result in oversizing of the PTO system. In addition, the oversizing of the PTO system can lead to inefficient operation of the system, as the generator may operate in a region where its efficiency is lower than its optimal operating point. This paper examines such extreme reactive power peaks in reactive WEC control with the help of analytical results and illustrative case studies.

A variety of specific studies document active and reactive power flows for particular WEC devices, under particular wave excitation conditions. However, no generic results or analysis is available to provide an understanding of why excessive reactive power leaks occur, or their origin. Some studies report excessive reactive power peaks with respect to active power peaks but fail to explain the rationale for such behaviour. For example, [11], [12] contain reports of reactive power flows in excess of the active power flow, under reactive force control, for a direct drive point absorber WEC using a hardware-in-the-loop (HiL) setup. Furthermore, there also exist reports of (average) negative power absorption (i.e. the WEC is an overall power *consumer*), which can be related to inappropriately timed or scaled reactive power peaks. For example, in [13], [14], the use of non-ideal PTO systems (i.e. having less than unity efficiency and usually containing nonlinear components), unrepresented in the WEC model used in the control system synthesis, results in overall negative power absorption. It is important to note that there are inevitable system/controller mismatches present in all real-world applications, which may result from modelling errors, controller synthesis errors or poor numerical controller implementation. The specific sources of mismatch impact the final performance of optimally controlled WECs, to a greater or lesser extent, in terms of power absorption and reactive power peak requirements, e.g. in [15] uncertainty in the system dynamic model results in negative power absorption. Additionally, sensor faults can result in higher reactive power peaks, as presented in [16] (velocity sensor error). While these anecdotes help to raise the alarm in relation to the necessity for extreme reactive power peaks, and the potential provision of excessive power ratings to cater for them, they do not yet give a wholesome understanding of their origin, or whether they should be provided for.

This paper derives general analytical results regarding the ratio of reactive-to-active power peaks for both monochromatic and panchromatic wave excitation, which are then

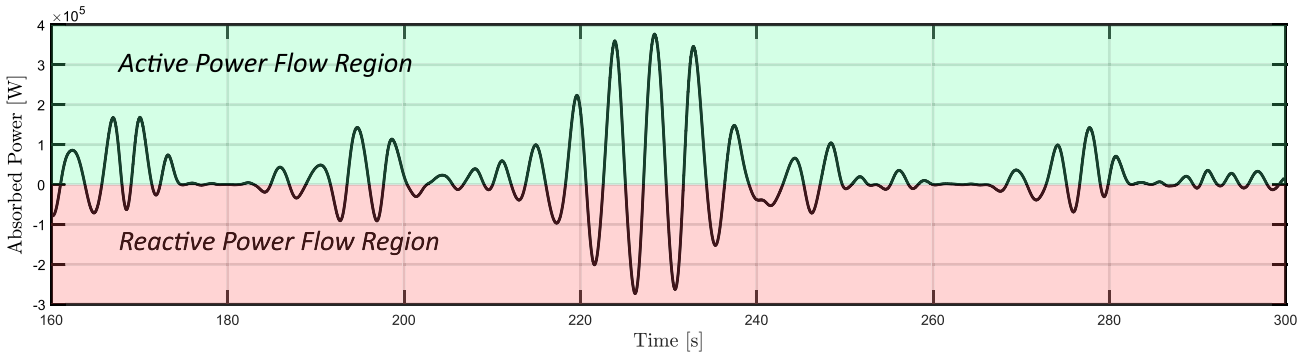

FIGURE 2. **A typical instantaneous power flow profile for an optimally controlled WEC operating in irregular waves. The green shaded region represents active power flow region, while the red shaded region represents reactive power flow region. However, mean power flow (energy) is positive overall.**

validated by a comprehensive set of simulation results. Monochromatic waves are characterised by a single frequency or period, whereas a (more realistic) panchromatic wave spectrum is continuous in frequency and encompasses an infinite number of spectral components, forming a continuous spectrum. In addition, model/controller mismatch cases are also considered and shown to be *the sole reason* for reactive-to-active power peak ratios above unity. It is essential to clarify that the term 'model/controller' mismatch encompasses both modelling errors and errors related to the controller synthesis procedure, as elaborated in Section V-B. Armed with this information, WEC developers have solid information on which to decide on appropriate levels of PTO (active and reactive) power capacity. This important result also clearly motivates the use of accurate and validated models (validated under controlled conditions [17]) for WEC controller synthesis. For cases where model/controller mismatch persists, it is yet unclear how best to ameliorate excessive reactive power peaks, though some studies have developed methods to include a reactive power limit as a nonlinear constraint, within the solution of the optimal WEC control problem [18]. However, without a clear explanation for the origin of excessive reactive power peaks, setting the reactive power limit remains an uncertain exercise.

The main contributions of the paper are summarised below:

- Analytical results, regarding the ratio of reactive-to-active power peaks, are derived for both monochromatic and panchromatic waves.
- Validation of the analytical results by a comprehensive selection of simulation results.
- Furthermore, the paper delves into mismatch cases (both in modelling and control), shedding light on the fact that such mismatches are the *sole reason* behind reactive-to-active power peak ratios exceeding unity. Some discussion considers how this situation may be addressed.

The remainder of the paper is organised as follows. Section II describes the modelling of a generic WEC system, while Section III discusses well-established optimal WEC control approaches based on the impedance-matching principle, including two finite-order realisations, which are adopted for the illustrative case studies (as detailed below). Reactive power peak analysis, including the derivation of analytical results, is presented in Section IV, while Section V presents illustrative case studies for both matched and mismatched cases (control synthesis and modelling errors). Section VI provides a comprehensive discussion on the significance of the result while, in Section VII, the conclusions of this study are drawn.

A. NOTATION AND CONVENTIONS

$\mathbb{R}^+(\mathbb{R}^-)$ denotes the set of non-negative (non-positive) real numbers. $(Z(\omega), z(t))$ denotes a Fourier transform pair. $G^\star(\omega)$ denotes the complex conjugate of $G(\omega)$. $\mathbb{Re}(H)$ and $\mathbb{Im}(H)$ indicate the real and imaginary-parts of the complex-valued function $H(\omega)$. The notation $\text{diag}(A_p)_{p=1}^N$, with $A_p \in \mathbb{C}^{n\times n}$, is used to denote the block-diagonal matrix associated to the set of matrices $\{A_p\}_{p=1}^N$, i.e.,

$$\text{diag}(A_p)_{p=1}^N = \begin{bmatrix} A_1 & 0 & \dots & 0 \\ 0 & A_2 & \dots & 0 \\ \vdots & \vdots & \ddots & \vdots \\ 0 & 0 & \dots & A_N \end{bmatrix} \in \mathbb{R}^{nN\times nN}.$$

Finally, when required, the abbreviations $\text{c}_\omega \equiv \cos(\omega t)$ and $\text{s}_\omega \equiv \sin(\omega t)$ are adopted for notational convenience.

II. WEC SYSTEM MODEL

As mentioned in Section I, WECs are devices used to harvest energy from ocean waves; therefore, it is essential to note that these 'converters' are different from 'converters' in the power electronic sense as they serve distinct purposes. In this section, we recall some fundamental concepts of WEC hydrodynamic modelling, based on linear potential flow theory [19] and the assumptions associated with this theory i.e., the fluid is incompressible, inviscid and irrotational. These assumptions are consistent with well-established practices in the WEC literature, particularly within the field of control engineering, and are rooted in Cummins' equation [20], a well-established framework for analysing WEC dynamics [5]. Although there

is a known challenge of control-induced motion exaggeration in WEC systems, referred to as the"modelling paradox" [17] in the literature. However, it is crucial to acknowledge that beginning with a simplified linear model analysis is necessary as it allows for concise analytical results. While it would be ideal to extend these findings to more realistic nonlinear cases, that is beyond the scope of this fundamental, and pioneering, study. The dynamics of the WEC, in the time domain, can be represented by the following equation of motion:

$$M\ddot{z}(t) + f_r(t) + f_h(t) = f_{\text{ex}}(t) - f_u(t), \tag{1}$$

where $f_{\text{ex}}(t)$ is the uncontrollable (and unmeasurable) excitation force due to the incoming wave field, $f_r(t)$ is the radiation force, and $f_h(t)$ is the linearised hydrostatic stiffness force. $f_u(t)$ represents the control force applied by the PTO system. M is the mass of the oscillating WEC, while $z(t)$, $\dot{z}(t) = v(t)$, and $\ddot{z}(t)$ represent heave displacement, velocity and acceleration, respectively. Additionally, (1) does not consider nonlinear hydrodynamic effects, such as viscous damping. The hydrostatic stiffness force is given by

$$f_h(t) = K_{\text{h}} z(t), \tag{2}$$

where $K_{\text{h}} > 0$ is the hydrostatic stiffness coefficient. The radiation force $f_r(t)$, which represents the fluid force induced by the body motion in generating waves, is modelled using Cummins' equation [20], as follows:

$$f_r(t) = h_r(t) * \dot{z}(t), \tag{3}$$

where $h_r(t)$ denotes the radiation convolution kernel. It is worth noting that general foundations of optimal energy maximising control for WEC systems, known in the literature as impedance-matching (or complex-conjugate) principle, are given normally in the frequency domain, rather than the time domain. Thus, $h_r(t)$ can be effectively described in the frequency domain by means of Ogilvie's relations [21], as:

$$\begin{cases} A_r(\omega) = m_\infty - \frac{1}{\omega}\int_0^{+\infty} h_r(t)\sin(\omega t)dt, \\ B_r(\omega) = \int_0^{+\infty} h_r(t)\cos(\omega t)dt. \end{cases}, \tag{4}$$

with $A_r(\omega) \in \mathbb{R}$ and $B_r(\omega) \in \mathbb{R}^+$ denoting the so-called radiation added-mass and damping, respectively. In addition, it must be noted that (4) verifies that $m_\infty = \lim_{\omega\to\infty} A_r(\omega)$. Then, using (4), the full frequency domain characterisation of $h_r(t)$ is given by:

$$H_r(\omega) = B_r(\omega) + \jmath\omega\left[A_r(\omega) - m_\infty\right]. \tag{5}$$

Thus, using fundamental properties of the Laplace transform and (4), the full force-to-velocity mapping for the model in (1) can be represented [22] as follows:

$$G(s) = \frac{s}{s^2(M + m_\infty) + s\hat{H}_r(s) + K_{\text{h}}}, \tag{6}$$

where $\hat{H}_r(s)$, which denotes a linear time-invariant approximation of $H_r(\omega)$, defined in (5), is generally obtained using generic boundary-element tools, such as NEMOH [23] (assuming infinite water depth), in combination with standard system identification toolboxes such as, for example, the FOAMM toolbox [24] for high fidelity approximation. In summary, our WEC model, as defined in (6), used for analysis, is driven by the necessity to develop fundamental analytical results. Initially, this approach is preferred as it allows for the derivation of essential analytical insights. However, the results nevertheless highlight the potential problem of using a linear controller with a real WEC, which exhibits nonlinearity (see, for example, Section V-B).

It must be noted that real WEC systems, described as in (6), are characterised to satisfy the properties of stability and passivity [25]. In particular, the system $G(s)$, in (6), is connected with the "intrinsic impedance" of WEC systems, $Z_i(\omega)$, as:

$$Z_i(\omega) = B_r(\omega) + \jmath\omega\left(M + A_r(\omega) - \frac{K_{\text{h}}}{\omega^2}\right) \approx \frac{1}{G(\jmath\omega)}, \tag{7}$$

where the approximation is a consequence of the radiation kernel approximation, i.e., $H_r(\omega) \approx \hat{H}_r(\jmath\omega)$. Then, the force-to-velocity description in (6) can be analogously expressed in terms of $Z_i(\omega)$, as follows:

$$V(\omega) = \frac{1}{Z_i(\omega)}\left[F_{\text{ex}}(\omega) - F_u(\omega)\right]. \tag{8}$$

It is worth mentioning that the expressions in (6)–(8), provide the optimal control foundations for WEC systems, presented in Section III.

III. OPTIMAL WEC CONTROL

Within the general optimal control problem for WEC systems, the main goal is to maximise the energy extracted from ocean waves, as efficiently as possible. To achieve this, the control input, $f_u(t)$, must be properly commanded through the PTO system, as required by the energy maximising control algorithm. A theoretical optimal complex-conjugate (Impedance-matching) controller, along with two finite order realisations, i.e., the **Li**near **Ti**me invariant **Con**troller (LiTe-Con) [22] and the reactive Proportional-Integral (PI) controller [5], are described in this section. Furthermore, a brief discussion is provided on possible system/controller mismatch caused by controller synthesis procedures used for finite order realisations.

A. THEORETICAL OPTIMUM

The general energy maximising control problem for WECs can be informally posed as follows [5]:

$$\underset{f_u(t)}{\text{Maximise}} \quad \text{Energy absorption from incoming waves.}$$

Then, from a mathematical perspective, the absorbed energy $\mathscr{J}$, over the time interval $[0,\ T]$, with $T \in \mathbb{R}^+$, can be expressed as:

$$\mathscr{J} = \int_0^T P_{abs}(t)dt, \tag{9}$$

where $P_{abs}(t) = v(t)f_u(t)$ denotes the instantaneous mechanical absorbed power, and $v(t)$ and $f_u(t)$ are the WEC velocity and control force, respectively with $v(t) = \dot{z}(t)$. Thus, under the general assumptions considered in Section II, the general

solution for the energy maximising control problem can be stated in terms of the optimal control force profile [5], as follows:

$$F_u^{opt}(\omega) = Z_i^{\star}(\omega)V(\omega). \tag{10}$$

Analogously, the impedance-matching condition can be expressed, in terms of an optimal velocity profile, with a purely real mapping, as:

$$V^{opt}(\omega) = \frac{1}{Z_i(\omega) + Z_i^{\star}(\omega)}F_{\text{ex}}(\omega) = \frac{1}{2B_r(\omega)}F_{\text{ex}}(\omega). \tag{11}$$

Thus, (10) and (11) define the well-established impedance-matching condition [26], which is generally expressed in a feedback control form as $H^{opt}_{v\mapsto f_u}(\omega) = Z_i^{\star}(\omega)$, where the controller $H^{opt}_{v\mapsto f_u}(\omega)$ is placed in the feedback path. Both (10) and (11) are frequency dependent, indicating that either only a single wave frequency is handled (ACC controller, see e.g. [27]) or that the controller parameters are adapted with frequency to cater for the panchromatic case. As discussed in [22], the impedance-matching condition can be similarly expressed in a feedforward structure, using the wave excitation force as the input of the feedforward controller $H^{opt}_{f_{\text{ex}}\mapsto f_u}(\omega)$, i.e.,

$$F_u^{opt}(\omega) = -H^{opt}_{f_{\text{ex}}\mapsto f_u}(\omega)F_{\text{ex}}(\omega), \tag{12}$$

with,

$$H^{opt}_{f_{\text{ex}}\mapsto f_u}(\omega) = G(\jmath\omega)Z_i^{\star}(\omega)\left(1 + G(\jmath\omega)Z_i^{\star}(\omega)\right)^{-1}. \tag{13}$$

Even though the feedback form is a standard, and well-known, scheme for WEC control problems in the literature, the causality of $H^{opt}_{v\mapsto f_u}(\omega)$ does not allow for a practical implementation of the panchromatic controller [22], nor the implementation of effective constraint handling mechanisms [6]. To overcome the aforementioned limitations for the feedback form, as discussed in [22], it is useful to define the expressions in (12) and (13) using the real-part and imaginary-part operators [22], as follows:

$$H^{opt}_{f_{\text{ex}}\mapsto f_u}(\omega) = \frac{\mathbb{Re}(G) + \jmath\mathbb{Im}(G)}{2\mathbb{Re}(G)}, \tag{14}$$

where $\mathbb{Re}(G)$ and $\mathbb{Im}(G)$ denote the real and imaginary parts of $G(\jmath\omega)$, respectively. Thus, using the real- and imaginary-parts operators, the optimal mapping from $F_{\text{ex}}(\omega)$ and $V^{opt}(\omega)$, introduced in (11), can be equivalently re-defined as:

$$\frac{V^{opt}(\omega)}{F_{\text{ex}}(\omega)} = T^{opt}_{f_{\text{ex}}\mapsto v}(\omega) = \frac{\mathbb{Re}(G)^2 + \mathbb{Im}(G)^2}{2\mathbb{Re}(G)}. \tag{15}$$

It is important to note that the force-to-force mapping, i.e., f_{ex} to f_u mapping $H^{opt}_{f_{\text{ex}}\mapsto f_u}(\omega)$, in (14) corresponds to the feedforward control structure, while force-to-velocity mapping $T^{opt}_{f_{\text{ex}}\mapsto v}(\omega)$ in (15) represents the mapping between f_{ex} (or $F_{\text{ex}}(\omega)$ in the frequency domain) and $V^{opt}(\omega)$, which is unique regardless of the control scheme used (feedback or feedforward). Hence, the following two conditions

$$\begin{aligned}&\text{(C1) } T^{opt}_{f_{\text{ex}}\mapsto v}(\omega) = \mathbb{Re}(T^{opt}_{f_{\text{ex}}\mapsto v}) \in \mathbb{R}^+ \ \&\\ &\text{(C2) } \mathbb{Re}(H^{opt}_{f_{\text{ex}}\mapsto f_u}) = 1/2,\end{aligned} \tag{16}$$

hold, $\forall\omega \in \mathbb{R}$. Note that **(C1)** stems from the positive-real nature of the map G for the WEC application (see e.g. [28]), meaning that the G does not have any right half-plane zeros or poles. Furthermore, **(C2)** results from algebraic manipulation of (14). Both conditions, **(C1)** and **(C2)**, are utilised to substantiate the analytical findings presented in Section IV.

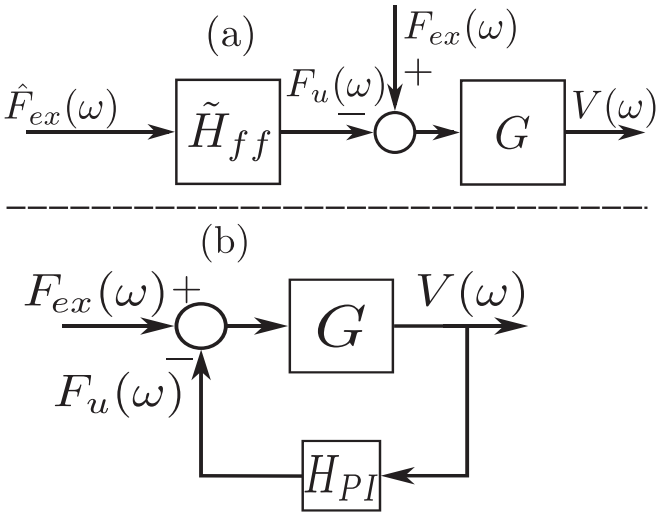

FIGURE 3. Control structures utilised in this paper. (a) Feedforward LiTe-Con structure. (b) Feedback Reactive PI structure.

B. LITE-CON

Using frequency-domain system identification algorithms [29], the LiTe-Con approximates $H^{opt}_{f_{\text{ex}}\mapsto f_u}(\omega)$, in (14), with an LTI-stable and implementable dynamical system $\tilde{H}_{\text{ff}}(s)$, i.e.:

$$\tilde{H}_{\text{ff}}(s)\Big|_{s=\jmath\omega} \approx H^{opt}_{f_{\text{ex}}\mapsto f_u}(\omega), \tag{17}$$

for $\omega \in [\omega_l,\ \omega_u]$, which represents the target frequency band for the controller approximation. Then, the resulting control force can be defined, in the frequency domain, as follows:

$$F_u(\omega) = -\tilde{H}_{\text{ff}}(\jmath\omega)F_{\text{ex}}(\omega). \tag{18}$$

With the definition in (17), the resulting force-to-velocity mapping is:

$$T^{LC}_{f_{\text{ex}}\mapsto v}(\jmath\omega) = \left(1 - \tilde{H}_{\text{ff}}(\jmath\omega)\right)G(\jmath\omega) \approx T^{opt}_{f_{\text{ex}}\mapsto v}(\omega), \tag{19}$$

for $\omega \in [\omega_l,\ \omega_u]$. The feedforward LiTe-Con control structure is shown in Fig. 3(a). The LiTe-Con provides a broadband control solution to effectively deal with panchromatic sea-states, where the power spectral density is mainly contained within $\mathcal{W} = [\omega_l,\ \omega_u]$. Tuning the LiTe-Con generally requires a global approximation using $\|\cdot\|_2$, rather than a focused

approximation using, for instance, the infinity norm. In order to do this, the following condition must be satisfied:

$$\|\tilde{H}_{\text{ff}}(\jmath\omega) - H^{opt}_{f_{\text{ex}}\mapsto f_u}(\omega)\|_2 < \epsilon,$$

where ϵ is an *'acceptability'* level defined as a design criterion. The *'acceptability'* of controller approximation depends upon the power absorption within the frequency band $\mathcal{W} = [\omega_l,\ \omega_u]$. Therefore, it is a design parameter aiming to maximise power absorption. The *'acceptability'* is usually specified by the user and verified through simulations. The interested readers are referred to [22] for a detailed discussion on LiTe-Con.

C. REACTIVE PI CONTROL

The so-called 'reactive' PI controller, represents a well-established standard feedback control solution within the WEC literature, as illustrated in Fig. 3(b). The control force is computed as a standard linear combination of the position and velocity of the WEC system:

$$f_u(t) = \begin{bmatrix} k_z & k_v \end{bmatrix} \begin{bmatrix} z(t) \\ \dot{z}(t) \end{bmatrix}, \tag{20}$$

which, using standard properties of the Laplace transform, can be written as

$$H_{PI}(s) = \frac{k_z s + k_v}{s}, \tag{21}$$

while the representation of the control force in the frequency domain is given by:

$$F_u(\omega) = -H_{PI}(\jmath\omega)V(\omega). \tag{22}$$

Throughout the WEC literature, this family of controllers is commonly tuned using exhaustive search procedures, assessing the resulting performance, measured in terms of absorbed energy, in a sufficiently large grid of values for k_z and k_v. However, based on the impedance-matching condition, discussed in Section III-A, analytical conditions can be given to maximise the absorbed energy, in unconstrained scenarios with monochromatic waves. Thus, the reactive PI controller parameters can be computed as follows:

$$k_z = \mathbb{R}\mathrm{e}\left\{\Gamma(\omega^*)\right\}, \quad k_v = -\omega^* \mathbb{I}\mathrm{m}\left\{\Gamma(\omega^*)\right\} \tag{23}$$

with,

$$\Gamma(\omega^*) = \frac{1}{T^{opt}_{f_{\text{ex}}\mapsto v}(\omega^*)} - \frac{1}{G(\jmath\omega^*)}, \tag{24}$$

and ω^* a particular frequency, where the energy absorption maximisation is targeted. Thus, the impedance-matching condition is satisfied for ω^* with $H_{PI}(s)$, for $s = \jmath\omega$, $\omega \in \mathbb{R}^+$. Thus, using the reactive PI controller structure defined in (20) and (24), the resulting force-to-velocity mapping results in a band-pass (resonant) system, for which the resonance frequency is ω^*, while its frequency response matches the optimal mapping $T^{opt}_{f_{\text{ex}}\mapsto v}(\omega)$ only for $\omega = \omega^*$, preserving the zero phase-locking given by the purely real mapping in (11). It is worth mentioning that, with the parameter definitions in (23), the resulting force-to-velocity mapping can be expressed as follows:

$$T^{PI}_{f_{\text{ex}}\mapsto v}(\jmath\omega^*) = \frac{G(\jmath\omega^*)}{1 + G(\jmath\omega^*)H_{PI}(\jmath\omega^*)} = T^{opt}_{f_{\text{ex}}\mapsto v}(\omega^*). \tag{25}$$

Finally, it must be noted that this family of controllers, defined using the expressions in (23), provides a narrow-banded control solution, which means that it is optimal for monochromatic waves with a significant performance degradation in scenarios with panchromatic waves.

D. CONTROL DESIGN MISMATCH

From a general perspective, analysing the WEC control problem in the frequency domain, there is an inherent mismatch between the optimal impedance-matching condition (see, for example (11)) and that is practically achievable with any existing energy maximising control solution for WEC systems. The inherent dynamical limitations include:

1) Non-causality (or anti-causality within this context), which is intrinsically related to stability issues [30] of impedance-matching-based controllers, must be mentioned as their most prominent limitation.
2) Bandwidth limitations in standard control solutions, represent another structural issue. By way of example, the reactive PI controller can optimally handle monochromatic waves, but not panchromatic sea-states, as discussed in Section III-C.

To achieve feasible control solutions, impedance-matching-based controllers simplify the WEC control problem using a (band-limited) frequency domain approximation. While optimisation-based controllers use finite order basis functions, such as a zero-order hold for MPC control, or Fourier basis functions for spectral or moment-based controllers, to simplify the control problem, which, in essence, is an infinite order control problem. Thus, each finite order control solution available in the literature has its strengths and weaknesses. In this study, the focus is on two performance impacts resulting from controller mismatch. Firstly, the impact of controller mismatch on reactive power demand is analysed. Secondly, the control performance, from a more traditional perspective, i.e., energy absorption, is studied. Finally, the link between these two aspects is examined.

IV. REACTIVE POWER PEAKS ANALYSIS

In this section, analytical results are derived for the matched optimal WEC control conditions presented in Section III-A.

A. PRELIMINARIES

Consistent with standard numerical generation methods for ocean waves (see e.g. [31]), we assume, in the following, that the wave excitation force, in the time-domain, can be represented as a T_0-periodic function defined on an N-dimensional space, written, without any loss of generality, as

$$f_{\text{ex}}(t) = \sum_{p=1}^{N} \alpha_p \cos(p\omega_0 t) - \beta_p \sin(p\omega_0 t), \tag{26}$$

with $\omega_0 = 2\pi/T_0$ the fundamental frequency associated with $f_{\text{ex}}(t)$. Note that $f_{\text{ex}}(t)$ can be written, in compact form, as

$$f_{\text{ex}}(t) = L_f \xi(t), \tag{27}$$

with $\{L_f^\mathsf{T}, \xi(t)\} \subset \mathbb{R}^{2N}$ defined as

$$L_f = \begin{bmatrix} \alpha_1 & \beta_1 & \dots & \alpha_N & \beta_N \end{bmatrix},$$
$$\xi(t) = \begin{bmatrix} \mathrm{c}_{\omega_0} & -\mathrm{s}_{\omega_0} & \dots & \mathrm{c}_{\omega_N} & -\mathrm{s}_{\omega_N} \end{bmatrix}^\mathsf{T}. \tag{28}$$

Remark 1: The condition $\xi(t) \neq 0$ holds for any $t \in \mathbb{R}$. This is, in fact, linked to the persistence of excitation condition on the set of functions composing the entries of ξ.

With the definition of f_{ex} in (27), and following similar arguments to those in e.g. [32], the time-domain equivalent of $V^{opt}(\omega)$ and $F_u^{opt}(\omega)$ in (11) and (12) can be written in terms of (27) as

$$v(t) = L_f \Phi_T \xi(t), \quad f_u(t) = L_f \Phi_H \xi(t), \tag{29}$$

with $\{\Phi_T, \Phi_H\} \subset \mathbb{R}^{2N \times 2N}$ defined as

$$\Phi_T = \operatorname{diag}\left(\begin{bmatrix} T^{opt}_{f_{\text{ex}} \mapsto v}(p\omega_0) & 0 \\ 0 & T^{opt}_{f_{\text{ex}} \mapsto v}(p\omega_0) \end{bmatrix} \right)_{p=1}^{N},$$

$$\Phi_H = \operatorname{diag}\left(\begin{bmatrix} 1/2 & \mathbb{Im}(H^{opt}_{f_{\text{ex}} \mapsto f_u}(p\omega_0)) \\ -\mathbb{Im}(H^{opt}_{f_{\text{ex}} \mapsto f_u}(p\omega_0)) & 1/2 \end{bmatrix} \right)_{p=1}^{N}. \tag{30}$$

Remark 2: Given the set of conditions **(C1)** and **(C2)** in (16), it is straightforward to check that the matrices Φ_T and Φ_H in (30) are always full rank. This result is leveraged in Section IV-B, to prove a set of results regarding instantaneous power absorption.

We now show that the instantaneous power $P_{abs}(t)$ can be written in terms of a time-dependent quadratic form. In particular, leveraging expressions in (27) and (29), note that

$$P_{abs}(t) = \left(L_f \Phi_T \xi(t)\right)\left(L_f \Phi_H \xi(t)\right)^\mathsf{T} = L_f A(t) L_f^\mathsf{T}, \tag{31}$$

where the matrix $A(t) \in \mathbb{R}^{2N \times 2N}$ is defined as[2]

$$A = \Phi_T \xi \xi^\mathsf{T} \Phi_H^\mathsf{T} = \Phi_T \Xi \Phi_H^\mathsf{T}, \tag{32}$$

with $\Xi = \xi\xi^\mathsf{T}$.

B. INSTANTANEOUS POWER CALCULATIONS

Before stating our main proposition, we provide a series of relevant intermediate results, in the following paragraphs. We begin by noting that the matrix A in (32) can be written, without any loss of generality, as

$$A = \underline{A} + \overline{A}, \tag{33}$$

where

$$\underline{A} = \tfrac{A + A^\mathsf{T}}{2}, \quad \overline{A} = \tfrac{A - A^\mathsf{T}}{2}, \tag{34}$$

with $\underline{A} = \underline{A}^\mathsf{T}$, $\overline{A} = -\overline{A}^\mathsf{T}$, the symmetric and skew-symmetric parts of A, respectively. Due to the quadratic nature of (31), it is straightforward to show that

$$P_{abs} = L_f A L_f^\mathsf{T} = L_f \left(\underline{A} + \overline{A}\right) L_f^\mathsf{T} = L_f \underline{A} L_f^\mathsf{T}. \tag{35}$$

We now state our first two relevant propositions. These are useful to prove our main statement (Proposition 3), which provides a relation between minimum and maximum active instantaneous power absorption.

Proposition 1: Consider $\underline{A}$ as in (35). Then, $\operatorname{rank}(\underline{A}) \leq 2$, for any $t \in \mathbb{R}$.

Proof: We first note that Ξ in (32) is, in fact, an outer product operation, and hence $\operatorname{rank}(\Xi) = 1$ for every possible ξ, since $\xi \neq 0\ \forall t$ (see Remark 1). Our proof then follows standard rank arguments in finite-dimensional spaces, i.e., note that

$$\begin{aligned} \operatorname{rank}(A) &= \operatorname{rank}(\Phi_T \Xi \Phi_H^\mathsf{T}) \\ &\leq \min\left(\operatorname{rank}(\Phi_T), \operatorname{rank}(\Xi), \operatorname{rank}(\Phi_H)\right) \\ &= \min(2N, 1, 2N) = 1, \end{aligned} \tag{36}$$

since both Φ_T and Φ_H are always full rank (see Remark 2). Finally,

$$\operatorname{rank}(\underline{A}) = \operatorname{rank}(A + A^\mathsf{T}) \leq 2 \operatorname{rank}(A) = 2, \tag{37}$$

which proves our claim. ■

Proposition 2: The trace of the matrix $\underline{A}$, denoted as $tr(\underline{A})$, is always positive for all $t \in \mathbb{R}$.

Proof: Firstly, note that it is straightforward to show that $\operatorname{tr}(\underline{A}) = \operatorname{tr}(A)$. With standard algebraic manipulation of A, it is possible to show that its set of diagonal elements, denoted as $d(A) \subset \mathbb{R}$, is composed of the union of two sets, i.e.,

$$d(A) = d_1 \cup d_2, \tag{38}$$

where the sets d_1 and d_2 are

$$d_1 = \left\{ T^{opt}_{f_{\text{ex}} \mapsto v}(p\omega_0) \left(\tfrac{1}{2}\mathrm{c}^2_{p\omega_0} - \mathbb{Im}(H^{opt}_{f_{\text{ex}} \mapsto f_u}(p\omega_0)) \mathrm{c}_{p\omega_0} \mathrm{s}_{p\omega_0} \right) \right\}_{p=1}^{N},$$

$$d_2 = \left\{ T^{opt}_{f_{\text{ex}} \mapsto v}(p\omega_0) \left(\tfrac{1}{2}\mathrm{s}^2_{p\omega_0} + \mathbb{Im}(H^{opt}_{f_{\text{ex}} \mapsto f_u}(p\omega_0)) \mathrm{c}_{p\omega_0} \mathrm{s}_{p\omega_0} \right) \right\}_{p=1}^{N}. \tag{39}$$

By using the formal definition of trace, i.e., the sum of the elements in $d(A)$, note that

$$\begin{aligned} \operatorname{tr}(A) &= \sum_{p=1}^{N} \tfrac{1}{2} \left(\mathrm{c}^2_{p\omega_0} + \mathrm{s}^2_{p\omega_0} \right) T^{opt}_{f_{\text{ex}} \mapsto v}(p\omega_0) \\ &= \sum_{p=1}^{N} \tfrac{1}{2} T^{opt}_{f_{\text{ex}} \mapsto v}(p\omega_0), \end{aligned} \tag{40}$$

[2]From now on, we omit the dependence on t when it is clear from the context.

which is strictly positive for all $t \in \mathbb{R}$ (since (40) is, in fact, independent of t), due to condition **(C1)** in (16), which proves our claim. ■

Having introduced Propositions 1 and 2, we define the following main relevant quantities in terms of (31). Let P^l and P^u be

$$P^l = \min_{L_f} \frac{1}{\|L_f\|^2} L_f \underline{A} L_f^{\mathsf{T}}, \quad P^u = \max_{L_f} \frac{1}{\|L_f\|^2} L_f \underline{A} L_f^{\mathsf{T}}, \tag{41}$$

i.e., the (normalised) *minimum* and *maximum* achievable value of instantaneous power P_{abs} under optimal controlled conditions, for any admissible wave excitation force vector $L_f^{\mathsf{T}} \in \mathbb{R}^{2N}$, and $t \in \mathbb{R}$. That is, for every possible wave excitation force realisation L_f, according to a given spectrum (see Section V). It is essential to note that we include this normalisation factor to ensure that the problem is well-posed. Without normalisation, the variable L_f could take arbitrarily large values, which is never the case in practice. Furthermore, we introduce the definition of the peak power ratio P_{ratio} as

$$P_{\text{ratio}} = \frac{|P^l|}{|P^u|}. \tag{42}$$

Our main proposition can be stated as follows.

Proposition 3: Let P^l and P^u be defined as in (41). Then, $P^u > 0$ for all $t \in \mathbb{R}$. Furthermore, $|P^u| > |P^l|$, and hence $P_{\text{ratio}} < 1$, for all $t \in \mathbb{R}$.

Proof: Suppose for the moment that the value of t is fixed to $t = t^*$. We first note that, using variational arguments (see [33]), the quantities P^l and P^u in (41) can be exactly computed in terms of the spectrum of $\underline{A}$, i.e.,

$$P^l = \min_{L_f} \frac{1}{\|L_f\|^2} L_f \underline{A} L_f^{\mathsf{T}} = \lambda^l,$$

$$P^u = \max_{L_f} \frac{1}{\|L_f\|^2} L_f \underline{A} L_f^{\mathsf{T}} = \lambda^u, \tag{43}$$

where[3] $\{\lambda^l, \lambda^u\} \subset \mathbb{R}$ are the smallest and largest eigenvalues of $\underline{A}$, respectively. Note that the instantaneous mechanical power can be negative for reactively controlled WEC. Therefore, λ^l can be negative as it represents the maximum reactive power peak, for all admissible L_f. By Proposition 1, $\text{rank}(\underline{A}) \leq 2$, and hence its spectrum can always be decomposed as

$$\lambda(\underline{A}) = \{\lambda^l, \lambda^u\} \cup \{\underbrace{0, \ldots, 0}_{2(N-1)}\}. \tag{44}$$

Furthermore, using the well-known property that the trace of a matrix equals the sum of its eigenvalues, the following relation

$$\text{tr}(\underline{A}) = \lambda^l + \lambda^u, \tag{45}$$

holds. Finally, by Proposition 2, we have

$$\text{tr}(\underline{A}) = \sum_{p=1}^{N} \tfrac{1}{2} T^{opt}_{f_{\text{ex}} \mapsto v}(p\omega_0) = \lambda^l + \lambda^u > 0, \tag{46}$$

and hence, clearly, $\lambda^u > 0$ and $|\lambda^u| > |\lambda^l|$ for any possible $t^* \in \mathbb{R}$ (since the trace condition (40) is indeed independent of time), which proves our main claim. ■

Remark 3: The result in Proposition 3 can be seen as a 'worst-case scenario' measure, and essentially states that the absolute value associated with the maximum instantaneous power achieved over the set of admissible L_f, i.e., $|P^u|$, is always larger than its minimum counterpart, i.e., $|P^l|$. Note that P^u and P^l do not, in general, take place for the same excitation force vector L_f. Furthermore, Proposition 3, clearly, does not imply that the instantaneous power for a given realisation is always positive for a given L_f, but rather states a relation between maximum and minimum values over admissible L_f vectors. This is illustrated via Fig. 4, where maximum and minimum (normalised with respect to P^u) instantaneous power values can be appreciated (left), for 500 random realisations of L_f vectors according to a typical wave spectrum, for the device presented in Section V, under optimal control conditions. Furthermore, a snippet of the time trace of instantaneous power corresponding with the realisation linked to P^u (centre) and P^l is offered (right), showing both maximum and minimum values attained (with circles). Note that, clearly, even for these limit-case realisations, reactive power flow is effectively present.

Remark 4: From the results of Proposition 3, we can deduce straightforwardly that the above results hold for the monochromatic case ($N = 1$ in (26)), i.e., $|\lambda^u| > |\lambda^l|$ and peak power ratio $P_{\text{ratio}} < 1$.

We address, in the following, particular cases of interest, in the form of Corollary 1 and Corollary 2.

Corollary 1 (Asymptotic cases): $\lambda^l \to -\lambda^u$ as $\omega_0 \to 0$ or $\omega_0 \to +\infty$.

Proof: We begin with the case $\omega_0 \to 0$, which follows immediately by noting that

$$\lim_{\omega_0 \to 0} \lambda^l + \lambda^u = \lim_{\omega_0 \to 0} \sum_{p=1}^{N} \tfrac{1}{2} T^{opt}_{f_{\text{ex}} \mapsto v}(p\omega_0) = 0, \tag{47}$$

due to the fact that $G(\jmath\omega)$ is zero at the origin, see [28], and hence $\lambda^l \to -\lambda^u$ as $\omega_0 \to 0$. A similar argument can be followed for the case $\omega_0 \to +\infty$ taking into account that $G(\jmath\omega)$ is strictly proper, and it is hence omitted. ■

Remark 5: The result of Corollary 1 essentially states that the ratio between the absolute value of the minimum and maximum achievable instantaneous power tends to 1, i.e., $P_{\text{ratio}} \to 1$, in the asymptotic cases $\omega_0 \to 0$ and $\omega_0 \to +\infty$.

Corollary 2: Let $N = 1$ and $\omega_0 = \omega_r$, where ω_r denotes the resonant frequency of the WEC system. Then, the smallest and largest eigenvalues of $\underline{A}$ are $\lambda^l = 0$ and $\lambda^u = \frac{1}{4}\mathbb{R}\text{e}(G(\omega_r))$.

Proof: First of all, note that, at resonance, $\mathbb{I}\text{m}(G(\omega_r)) = 0$, and hence

$$T^{opt}_{f_{\text{ex}} \mapsto v}(\omega_r) = \tfrac{1}{2}\mathbb{R}\text{e}(G(\omega_r)). \tag{48}$$

[3] We recall that the eigenvalues of a symmetric matrix are always real (see e.g. [33]).

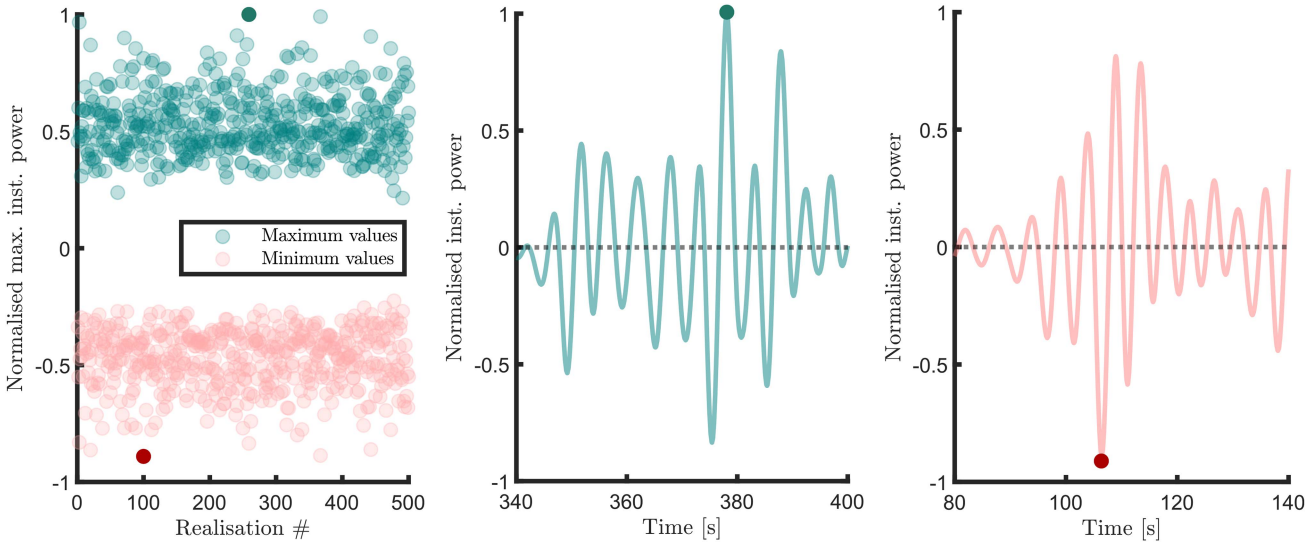

FIGURE 4. Maximum and minimum (normalised with respect to P^u) instantaneous power values for 500 random realisations of L_f vectors according to a typical wave spectrum, for the device presented in Section V, under optimal control conditions. Snippet of the time trace of instantaneous power corresponding with the realisation linked to P^u (centre) and P^l is offered (right), showing both maximum and minimum values attained (with circles).

Straightforward calculations show that $\underline{A}$ reduces to

$$\underline{A} = \tfrac{1}{4}\mathbb{R}\mathrm{e}(G(\omega_r))\begin{bmatrix} \mathrm{c}^2_{\omega_r} & -\mathrm{c}_{\omega_r}\mathrm{s}_{\omega_r} \\ -\mathrm{c}_{\omega_r}\mathrm{s}_{\omega_r} & \mathrm{s}^2_{\omega_r} \end{bmatrix}, \tag{49}$$

which has a characteristic polynomial $P_{\underline{A}}(\lambda)$ given by

$$P_{\underline{A}}(\lambda) = \tfrac{1}{4}\mathbb{R}\mathrm{e}(G(\omega_r))\lambda\,(\lambda - 1)\,. \tag{50}$$

Since $\mathbb{R}\mathrm{e}(G(\omega_r)) > 0$ given the positive-real nature of G, the smallest and largest eigenvalues of $\underline{A}$ are

$$\lambda^l = 0 \quad \wedge \quad \lambda^u = \tfrac{1}{4}\mathbb{R}\mathrm{e}(G(\omega_r)), \tag{51}$$

which proves the claim. ■

Remark 6: The result of Corollary 2 states one fundamental result from a practical standpoint: The minimum possible value for the instantaneous power, over the space of admissible excitation forces, at resonance *is always 0*, i.e., only active instantaneous power is required by the optimal control condition at ω_r.

C. ENERGY RESULTS

Let us recall the definition of absorbed mechanical energy $\mathscr{J}$ from (9), over a period T_0 as

$$\mathscr{J} = \int_0^{T_0} P_{abs}(t)\mathrm{d}t, \tag{52}$$

where P_{abs} defined as in (31)–(35), i.e., WEC instantaneous mechanical power under frequency-domain optimality conditions. We make the following proposition concerning $\mathscr{J}$.

Proposition 4: The mechanical energy $\mathscr{J}$ is strictly positive for any admissible excitation force vector $L_f \in \mathbb{R}^{1\times 2N}$.

Proof: Let us re-write (52) in terms of (35) as

$$\begin{aligned}\mathscr{J} &= \int_0^{T_0} L_f \Phi_T\, \Xi(t) \Phi_H^{\mathsf{T}} L_f^{\mathsf{T}} \mathrm{d}t \\ &= L_f \Phi_T \left(\int_0^{T_0} \Xi(t)\mathrm{d}t \right) \Phi_H^{\mathsf{T}} L_f^{\mathsf{T}},\end{aligned} \tag{53}$$

and note that the equality

$$\begin{aligned}\int_0^{T_0} \Xi(t)\mathrm{d}t &= \int_0^{T_0} \mathrm{diag}\left(\begin{bmatrix} c^2_{p\omega_0} & -c_{p\omega_0}s_{p\omega_0} \\ -c_{p\omega_0}s_{p\omega_0} & s^2_{p\omega_0} \end{bmatrix} \right)_{p=1}^{N} \mathrm{d}t \\ &= \frac{T_0}{2}\mathbb{I}_{2N},\end{aligned} \tag{54}$$

holds, since is each element of the matrix in (54) represents, effectively, a standard inner-product operation between a set of orthogonal functions in L^2. It suffices to note that, using (54), the mechanical energy can be expressed as

$$\mathscr{J} = \frac{T_0}{2} L_f \left(\frac{\Phi + \Phi^{\mathsf{T}}}{2} \right) L_f^{\mathsf{T}}, \tag{55}$$

where the matrix $\Phi \in \mathbb{R}^{2N\times 2N}$ is defined as

$$\begin{aligned}\Phi &= \Phi_T \Phi_H^{\mathsf{T}} \\ &= \mathrm{diag}\left(\begin{bmatrix} \frac{1}{2}T^{opt}_{f_{\mathrm{ex}}\mapsto v}(p\omega_0) & -\mathbb{I}\mathrm{m}(H^{opt}_{f_{\mathrm{ex}}\mapsto f_u}(p\omega_0)) \\ \mathbb{I}\mathrm{m}(H^{opt}_{f_{\mathrm{ex}}\mapsto f_u}(p\omega_0)) & \frac{1}{2}T^{opt}_{f_{\mathrm{ex}}\mapsto v}(p\omega_0) \end{bmatrix} \right)_{p=1}^{N}.\end{aligned} \tag{56}$$

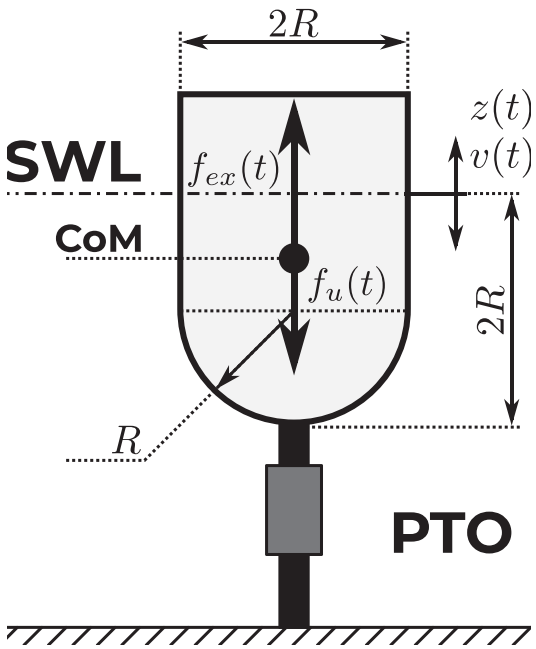

FIGURE 5. Schematic diagram of cylindrical WEC with hemispherical bottom. All the relevant dimensions are shown in the schematic, with $R = 5$ [m]. SWL and CoM represent the still water level and center of mass, respectively.

The claim then follows immediately from the fact that the symmetric matrix

$$\frac{\Phi + \Phi^{\mathsf{T}}}{2} = \operatorname{diag}\left(\begin{bmatrix} \frac{1}{2}T^{opt}_{f_{\text{ex}}\mapsto v}(p\omega_0) & 0 \\ 0 & \frac{1}{2}T^{opt}_{f_{\text{ex}}\mapsto v}(p\omega_0) \end{bmatrix}\right)_{p=1}^{N}, \tag{57}$$

in (55) is always positive-definite, due to condition **(C1)** in (16), and hence the mechanical energy $\mathscr{J}$ is always positive for any admissible excitation force vector L_f. ■

V. ILLUSTRATIVE CASE STUDIES

This section presents illustrative case studies to verify the analytical results presented in Section IV-B. The simulation results also illustrate the effects of possible system/controller mismatch on the peak power ratio and absorbed power. A single body floating WEC, oscillating in heave, is considered in this study. The schematic diagram of the considered WEC is shown in Fig. 5. Additionally, regarding the applicability of the proposed results to multi-mode (multi-degrees-of-freedom) devices, it is important to note that, in the majority of devices, there is only one controlled degree of freedom (DoF) [34]. However, exceptions exist, such as the ISWEC [35], which involve more than one controlled DoF. Nevertheless, the analytical findings presented in this paper primarily address the issue of reactive power peaks in the *controlled* DoF (or DoFs) of a device operating in realistic sea conditions, but specifically focusing on the heave DOF of a point absorber WEC as an illustrative case study. The analysis presented in this section considers both monochromatic and panchromatic wave conditions. The sea-states are characterised by a significant wave height $H_s = 3$ [m] and typical peak period $T_p \in [4, 20]$ [s] or typical peak frequency $\omega_p \in [0.31, 1.57]$ [rad/s], which cover the operation range of the considered WEC. A panchromatic wave spectrum is continuous and contains an infinite number of spectral components (i.e., a continuous spectrum), while a polychromatic representation includes a finite number of frequencies and is usually used for simulated wave synthesis. Therefore, a polychromatic representation with limited frequencies is used to approximate a panchromatic spectrum for simulation purposes here. For polychromatic (irregular) wave generation, a JONSWAP spectrum [36] is used to generate the corresponding free surface elevation, which is then used to calculate excitation force f_{ex}, through a wave-to-force convolution kernel obtained from the hydrodynamic parameters, computed using generic boundary-element methods-based tool NEMOH [23]. The corresponding spectral density function (SDF) of the JONSWAP spectrum is given below [36]:

$$S(\omega) = \frac{\alpha g^2}{\omega^5} exp\left[-\beta\frac{\omega_p^4}{\omega^4}\right]\gamma^{a(\omega)}, \tag{58}$$

where α and β are constant values, g is gravitational acceleration, $a(\omega)$ is a frequency dependent function, and γ is the peak enhancement factor, respectively. Moreover, to get statistically consistent results, 30 realisations of each sea-state are considered, and the length of time associated with each realisation is 300 times the typical peak wave period.

A. MATCHED CASES

The results presented in this section assume that the matched case holds, i.e., there is no mismatch (errors and uncertainties) between the nominal model, used for optimal control design, and the WEC system. Additionally, these results are computed under theoretically ideal conditions using a non-causal, optimal controller, presented in Section III-A. Fig. 6 presents the peak power ratio P_{ratio} for the range of wave frequencies considered. In particular, Fig. 6(a) presents results for the monochromatic case and Fig. 6(b) presents results for the panchromatic case, respectively. It is clear from Fig. 6 that the P_{ratio} never exceeds unity for both monochromatic and panchromatic cases, in accordance with the analytical results (see Proposition 3 and Remark 4). Moreover, $P_{\text{ratio}} \to 0$ as $\omega \to \omega_r$ of the device (see Corollary 2), which illustrates that the optimal controller does not require any reactive power at resonance under monochromatic wave excitation (Fig. 3(a)). Since panchromatic wave spectra are broadbanded, P_{ratio} never reaches zero at resonant frequency (it is, however, at minimum). Moreover, the *peakiness* of the spectrum, characterised by γ in (58), affects P_{ratio} as illustrated in Fig. 6(b). Increasing γ results in a more *peaky* spectrum, i.e., the spectrum is more concentrated around a peak frequency, with smaller effective bandwidth. It is worth mentioning that the $\gamma > 7$ is unusual for a JONSWAP spectrum. However, $\gamma > 7$

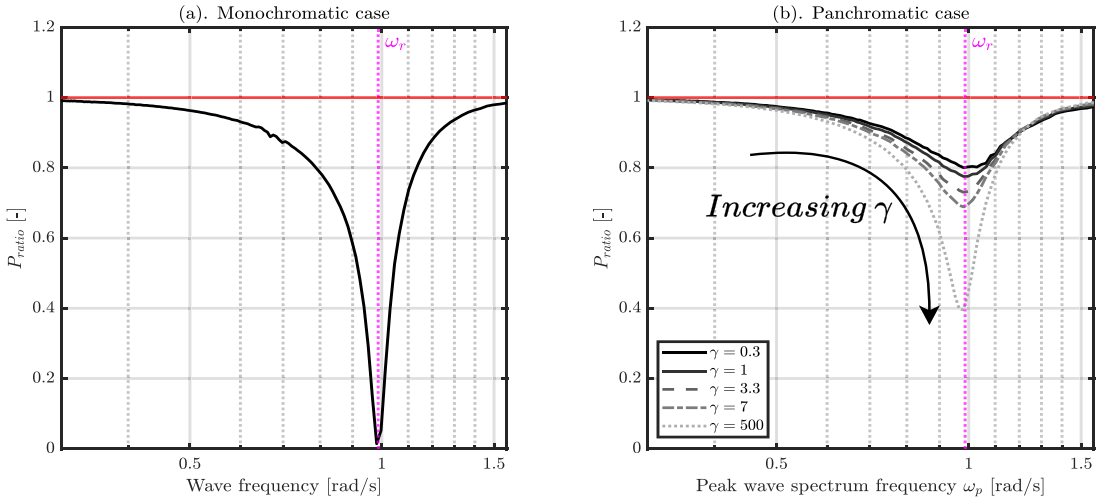

FIGURE 6. Peak power ratio P_{ratio}, for the range of wave frequencies considered, for optimal controller. (a) Monochromatic case. (b) Panchromatic case. The vertical purple dotted line depicts the resonant frequency ω_r of the WEC.

is used here to effectively demonstrate the impact of increasing γ on P_{ratio}. Unsurprisingly, P_{ratio} for increasing γ tends toward the monochromatic case, as shown in Fig. 6(b), since $\gamma \to \infty$ gives an effective monochromatic wave spectrum. It can also be seen, from Fig. 6, that P_{ratio} approaches 1 for asymptotic values of ω (i.e., $\omega \to 0, \infty$), which verifies the Corollary 1.

B. MISMATCHED CASES

Section V-A presents the case study results for a fully-matched case, from model and controller perspectives. However, there is always a mismatch present in practice. The mismatches stem from various sources, including unmodelled dynamics, modelling uncertainties, and also inherent approximation in the controller design synthesis procedure. In this section, we present two main types of mismatch cases, including modelling errors, also referred to as the *parametric mismatch*, and errors in the controller synthesis procedure, referred to as the *controller mismatch*.

1) MODELLING ERRORS (PARAMETRIC MISMATCH)

As discussed earlier in Section V-B, there is always a mismatch present in the WEC nominal model and actual system. One of the mismatches is the modelling uncertainties in the main hydrodynamic parameters. To illustrate the effect of modelling uncertainties in the WEC model, in the following, the main hydrodynamic parameters in the WEC model, i.e., mass M, hydrostatic stiffness K_{h} and radiation damping $B_r(\omega)$ may be subject to multiplicative modelling errors, as follows:

$$\begin{aligned} \hat{M} &= \delta m M, \\ \hat{K}_{\text{h}} &= \delta k K_{\text{h}}, \\ \hat{B}_r(\omega) &= \delta b B_r(\omega), \end{aligned} \tag{59}$$

where $[\delta m, \delta k, \delta b] \subset [0.5, 2]$, representing a variation of 50–200% in the hydrodynamic parameters M, K_{h} and $B_r(\omega)$, respectively. Indeed, for specific WEC types, large hydrodynamic modelling errors are not uncommon, and the significant reactive power peaks (with $P_{\text{ratio}} > 3$) have been reported in experimental studies, which suggests that such errors are not entirely uncommon. Now, as per the nominal WEC model introduced in (7), the real (mismatched) model $\hat{G}(j\omega)$, including parametric variations, can be represented as follows:

$$\hat{G}(j\omega) = \frac{1}{\hat{Z}_i(\omega)} = \frac{1}{\hat{B}_r(\omega) + j\omega(\hat{M} + A_r(\omega) - \frac{\hat{K}_{\text{h}}}{\omega^2})}. \tag{60}$$

The optimal impedance-matching condition $H^{opt}_{f_{\text{ex}} \mapsto f_u}(\omega)$, given in (13), is implemented on the real (mismatched) model $\hat{G}(j\omega)$, presented in (60). The process of implementing modelling errors is entirely conducted in the frequency domain, where all signals and dynamical system responses are expressed in their spectral representations, including the wave excitation force $f_{\text{ex}}(t)$, control force $f_u(t)$, velocity $v(t)$, and frequency responses of the systems like the real system $\hat{G}(j\omega)$ in (60), or the analysed control structure, such as the optimal feedforward control mapping $H^{opt}_{f_{\text{ex}} \mapsto f_u}(\omega)$. Using these spectral representations, we calculate all interactions according to their corresponding input-output relations. The time-domain signals are then obtained through an inverse Fourier transform.

Fig. 7 shows the effect of parametric variations on peak power ratios under various monochromatic waves. Specifically, Fig. 7(a) presents how the hydrostatic stiffness variations $\hat{K}_{\text{h}}$ affect P_{ratio} and it is evident, from Fig. 7, that $\hat{K}_{\text{h}}$ has a detrimental effect in terms of reactive power peak requirements, with some cases requiring reactive power peaks 47 times the active power peak. Similarly, mass variations $\hat{M}$ negatively impact P_{ratio}, with reactive power peaks almost 16 times the active power peak in a case, as shown in Fig. 7(b). On the other hand, the effects of radiation damping variations $\hat{B}_r(\omega)$ on P_{ratio} are not as detrimental as stiffness

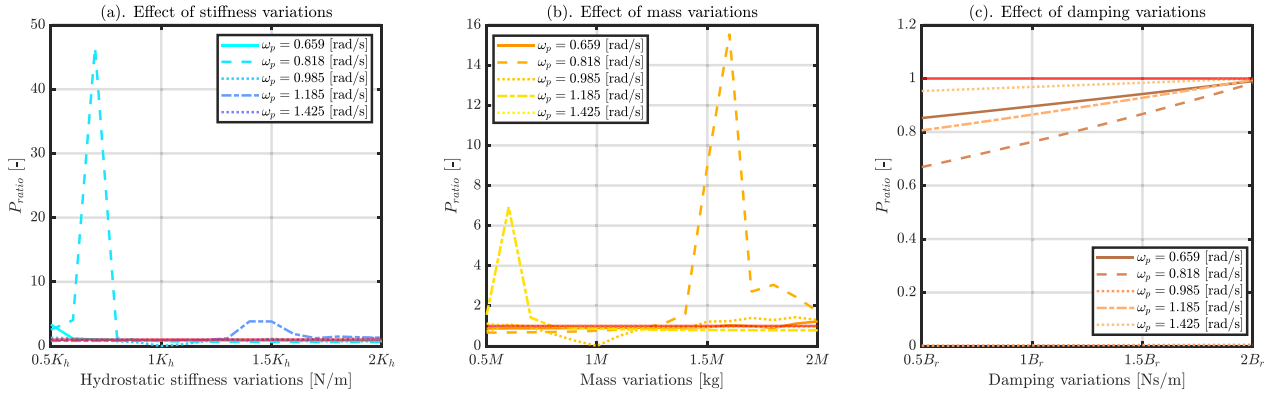

FIGURE 7. Effects of parametric mismatch on peak power ratio P_{ratio} for optimal controller under monochromatic waves: (a) Peak power ratio P_{ratio} for the range of hydrostatic stiffness variations $\hat{K}_h \in [0.5K_h, 2K_h]$ [N/m], where $K_h = 7.8868 \times 10^5$ [N/m]. (b) Peak power ratio P_{ratio} for the range of mass variations $\hat{M} \in [0.5M, 2M]$ [kg], where $M = 6.6792 \times 10^5$ [kg]. (c) Peak power ratio P_{ratio} for the range of damping variations $\hat{B}_r(\omega) \in [0.5B_r(\omega), 2B_r(\omega)]$ [Ns/m]. ω_p represents wave frequency.

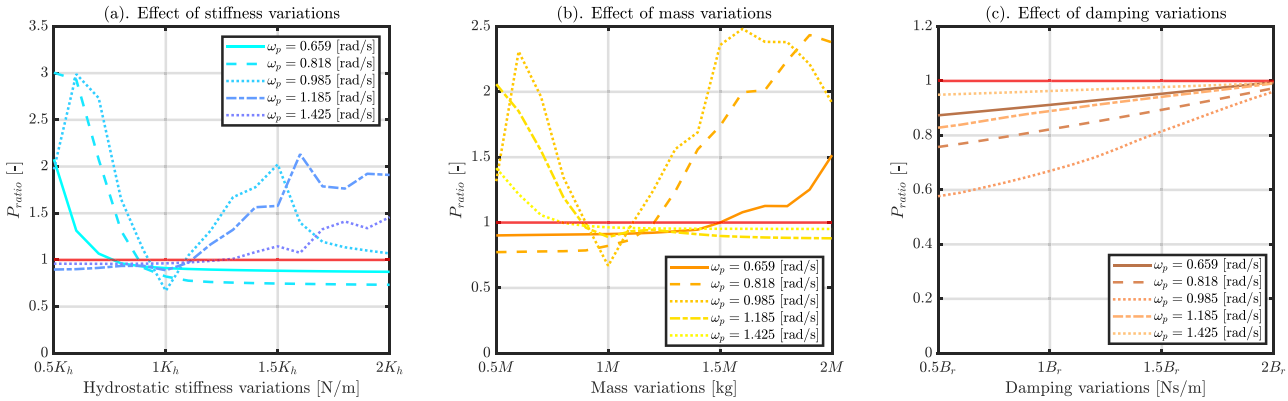

FIGURE 8. Effects of parametric mismatch on peak power ratio P_{ratio} for optimal controller under panchromatic waves: (a) Peak power ratio P_{ratio} for the range of hydrostatic stiffness variations $\hat{K}_h \in [0.5K_h, 2K_h]$ [N/m], where $K_h = 7.8868 \times 10^5$ [N/m]. (b) Peak power ratio P_{ratio} for the range of mass variations $\hat{M} \in [0.5M, 2M]$ [kg], where $M = 6.6792 \times 10^5$ [kg]. (c) Peak power ratio P_{ratio} for the range of damping variations $\hat{B}_r(\omega) \in [0.5B_r(\omega), 2B_r(\omega)]$ [Ns/m]. ω_p represents peak wave spectrum frequency.

and mass variations, as shown in Fig. 7(c). For the same variation in radiation damping $\hat{B}_r(\omega)$, P_{ratio} never exceeds 1, i.e., the reactive power peaks are always less than the active power peaks. However, it can be observed, from Fig. 7(c), that P_{ratio} increases with increasing $\hat{B}_r(\omega)$, and will exceed 1, for $\hat{B}_r(\omega) > 2B_r(\omega)$.

Similarly, Fig. 8 presents the results for parametric mismatch under panchromatic waves. As expected, the results are very similar to the monochromatic case. However, the reactive power peak magnitudes are significantly lower than in the monochromatic cases. In this case, $P_{\text{ratio}} \approx 3$ for stiffness variations $\hat{K}_{\text{h}}$, significantly less than $P_{\text{ratio}} \approx 47$ for the monochromatic case, in worst case scenario. Similar trends can be seen for the mass and damping variations ($\hat{M}$ and $\hat{B}_r(\omega)$) in Figs. 8(b) and 8(c), respectively.

It is essential to note that the effects of mass and stiffness variations depend on the incoming wave frequency (peak spectrum frequency for panchromatic cases) ω_p, relative to the WEC resonant frequency ω_r (≈ 0.987 [rad/s]). For $\omega_p < \omega_r$, stiffness variations $\hat{K}_{\text{h}}$ less than the nominal K_{h} result in higher P_{ratio}, while mass variations $\hat{M}$ greater than nominal mass M result in higher P_{ratio}. In contrast, for $\omega_p > \omega_r$, the effects on the P_{ratio} are opposite, i.e., for $\hat{K}_{\text{h}} > K_{\text{h}}$ and $\hat{M} < M$, effects are more prominent and lead to higher P_{ratio}. For $\omega_p \approx \omega_r$, however, the stiffness and mass variations adversely affect P_{ratio} irrespective of the variations in K_h and M, as shown in Figs. 7 and 8. On the other hand, no such effect is observed for radiation damping variations $\hat{B}_r(\omega)$, since radiation damping variations only affect the real part of the transfer function $\hat{G}(j\omega)$ given in (60) and, therefore, do not affect the phase of the system. Consequently, the effects of radiation damping are minimal, compared to mass and stiffness variations.

The effects of parametric mismatch on the absorbed power P_{abs}, compared to the optimal (fully-matched) case P_{opt}, is illustrated in Fig. 9. In particular, Fig. 9(a) shows the effect of stiffness variations $\hat{K}_{\text{h}}$ on the relative absorbed hydrodynamic power P_{abs}/P_{opt}, which depicts adverse effects of stiffness variations on the absorbed hydrodynamic power. Similarly, Fig. 9(b) depicts that mass variations impact absorbed

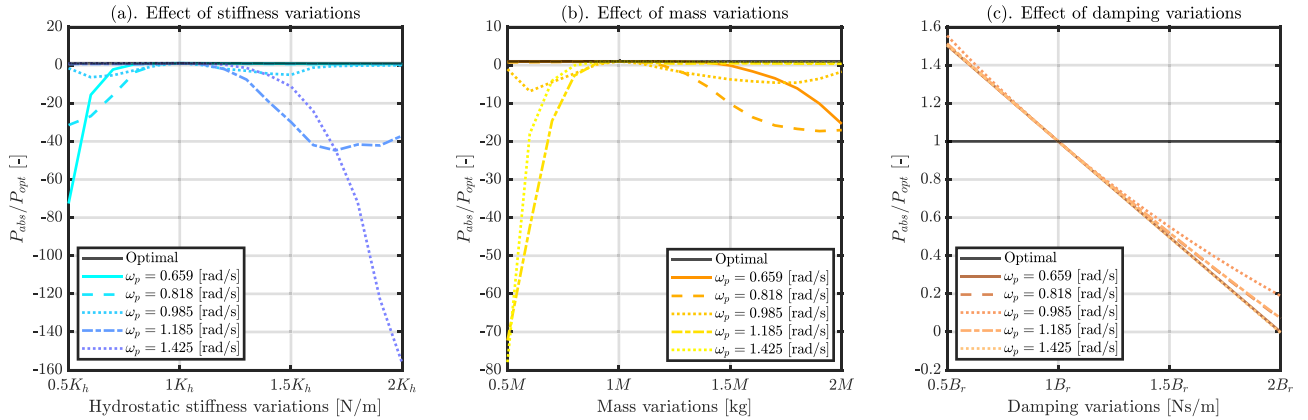

FIGURE 9. Effects of parametric mismatch on relative absorbed power P_{abs}/P_{opt} under panchromatic waves: (a) P_{abs}/P_{opt} for the range of hydrostatic stiffness variations $\hat{K}_h \in [0.5K_h, 2K_h]$ [N/m], where $K_h = 7.8868 \times 10^5$ [N/m]. (b) P_{abs}/P_{opt} for the range of mass variations $\hat{M} \in [0.5M, 2M]$ [kg], where $M = 6.6792 \times 10^5$ [kg]. (c) P_{abs}/P_{opt} for the range of damping variations $\hat{B}_r(\omega) \in [0.5B_r(\omega), 2B_r(\omega)]$ [Ns/m]. ω_p depicts the peak frequency of a wave spectrum, and P_{opt} represents the optimal absorbed power for fully matched case.

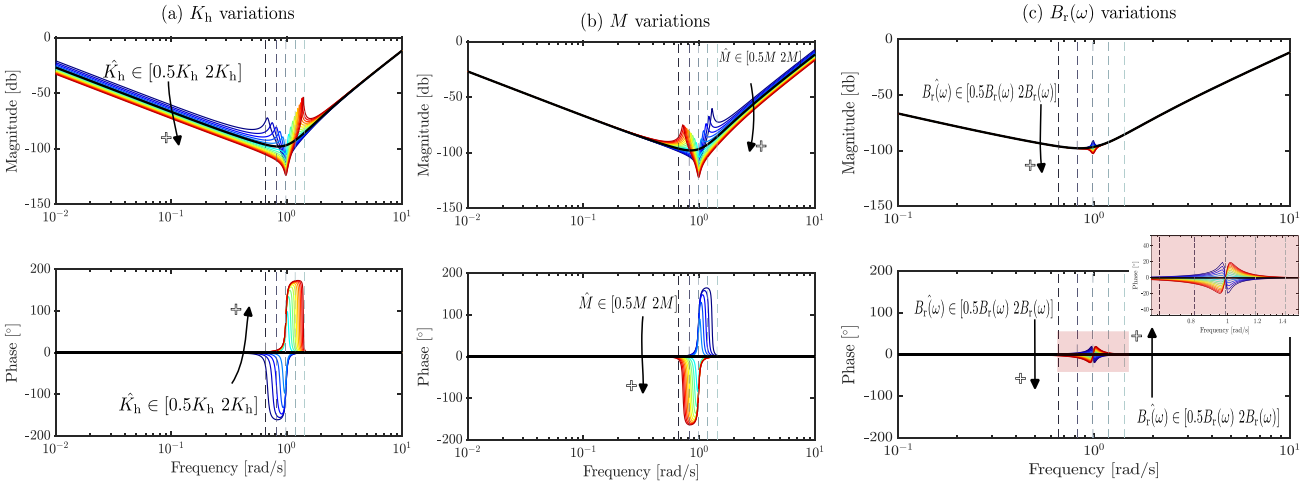

FIGURE 10. Effect of parametric variations on force-to-velocity response of the system. (a) Effect of stiffness variations. (b) Effects of mass variations. (c) Effects of damping variations. The dashed vertical lines represent incoming wave (peak spectrum) frequencies considered here.

hydrodynamic power adversely and result in overall negative power absorption for mismatch cases. It is also important to note that the magnitude of negative power absorption corresponds directly to the magnitude of the peak power ratio P_{ratio}, presented in Fig. 8. Additionally, the radiation damping variations $\hat{B}_r(\omega)$ affect the relative absorbed power slightly differently from the mass and stiffness variations. Specifically, for $\hat{B}_r(\omega) > B_r(\omega)$ variations, the relative absorbed power drops almost linearly. While, for $\hat{B}_r(\omega) < B_r(\omega)$ variations, a moderate increase in absorbed power is noted. However, it is worth mentioning that parametric uncertainties can also result in *higher* power absorption, as shown in [37]. Note that the effects of parametric variations on relative absorbed power, for monochromatic cases, are very similar to the panchromatic case, and therefore are not included, for brevity.

The somewhat erratic behaviour of the P_{ratio} in Figs. 7–9, especially for variations in K_h and M, are due to various effects. To illustrate these effects, Fig. 10 shows the force-to-velocity response of the system under parametric variations

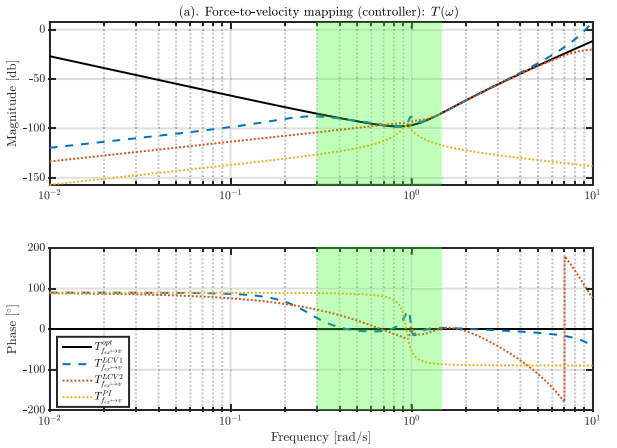

FIGURE 11. Force-to-velocity mapping $T(\omega)$ for the controllers considered here, *i.e, Optimal* $T^{opt}_{f_{ex}\mapsto v}$ (Black solid line), *LiTeCon-V1* $T^{LCV1}_{f_{ex}\mapsto v}$ (blue dashed line), *LiTeCon-V2* $T^{LCV2}_{f_{ex}\mapsto v}$ (orange dotted line), and *Reactive PI* $T^{PI}_{f_{ex}\mapsto v}$ (yellow dash-dot line), respectively. The shaded green region represents the wave frequency range considered for the analysis, i.e., the area of interest.

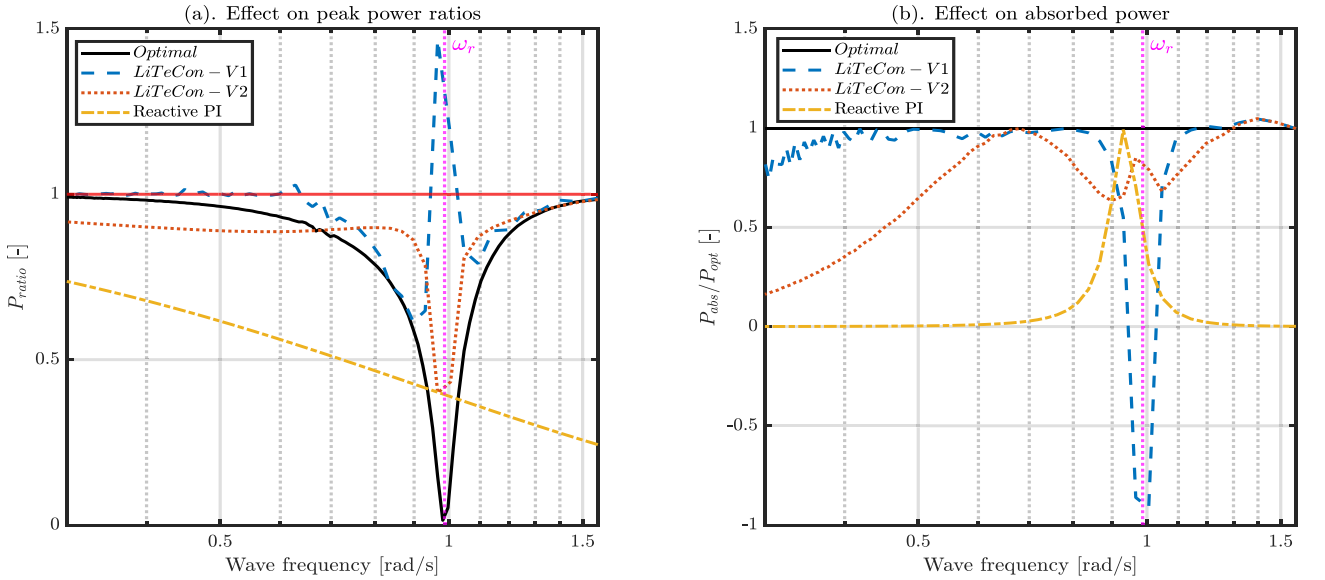

FIGURE 12. Effects of controller synthesis mismatch under monochromatic waves: (a) Peak power ratio P_{ratio} of three controllers for the range of wave frequencies considered. (b) Relative absorbed power P_{abs}/P_{opt} of the controllers for the range of wave frequencies considered. The vertical purple dotted line depicts the resonant frequency ω_r of the WEC.

such as stiffness K_h, mass M and damping $B_r(\omega)$ variations. It is clear from Fig. 10 that the K_h and M variations adversely affect the force-to-velocity response, especially the phase response, whereas the $B_r(\omega)$ variations have minimal effect, translating into the erratic behaviour of the results in Figs. 7–9. Additionally, the variations in K_h and M affect the phase response of the system, and can also be shown by (60), which shows that K_h and M make the imaginary part of the system $\hat{G}(j\omega)$ and, therefore, any variations in these quantities have adverse impacts on the phase response of the system. Finally, another important aspect that results in erratic behaviour in Figs. 7–9 is the position of the incoming wave peak (spectrum) frequency ω_p (relative to the device resonant frequency), illustrated by vertical dashed lines Fig. 10. Depending upon the value of ω_p, the parametric mismatch affects P_{ratio} differently. The worst case performance is achieved for $\omega_p = 0.818$ due to the highest phase difference between nominal and mismatched system models, as shown in Fig. 10(a) and (b).

2) CONTROLLER SYNTHESIS ERRORS (CONTROLLER MISMATCH)

In this section, the effects of controller synthesis mismatches on the reactive power requirements of a WEC, under controlled conditions, are examined. Controller mismatch arises due to the finite order realisation of the impedance-matching condition, as explained in Section III-D. Three finite order realisations, including two based on the LiTe-Con (namely *LiTeCon-V1* and *LiTeCon-V2*) controller and a *Reactive PI* controller, are considered here.

Fig. 11 presents the force-to-velocity response for each of the controllers considered here. Each controller tries to approximate the optimal impedance-matching force-to-velocity response $T^{opt}_{f_{\text{ex}}\mapsto v}$. Since each controller synthesis procedure is different, different approximation errors occur. Even for the same type of controller, i.e., LiTe-Con, the selection of different frequencies in the synthesis procedure results in two significantly different realisations and, therefore, disparate mapping characteristics, as illustrated in Fig. 11. Specifically, the force-to-velocity response $T^{LCV1}_{f_{\text{ex}}\mapsto v}$ outperforms $T^{LCV2}_{f_{\text{ex}}\mapsto v}$ in terms of correctly mapping the optimal force-to-velocity condition $T^{opt}_{f_{\text{ex}}\mapsto v}$, for the range of frequencies considered (shaded green region in Fig. 11). On the other hand, the *Reactive PI* controller maps just one frequency, as described in Section III-C, incurs the largest approximation error. It is important to note that all controllers struggle for fidelity around the resonant frequency, especially in capturing the phase response, which will affect the peak power requirements and is discussed in the following paragraphs.

Figs. 12 and 13 show how the controller mismatches, due to various controller synthesis procedures, adversely affect the peak power ratios P_{ratio} and relative absorbed power P_{abs}/P_{opt}, especially at frequencies where the controller force-to-velocity response does not capture the optimal force-to-velocity response (see Fig. 11). In particular, Fig. 12(a) presents P_{ratio} values for the three controller realisations, namely *LiTeCon-V1*, *LiTeCon-V2* and *Reactive PI* controller, compared with the optimal fully matched case (*Optimal*), under monochromatic waves. Note that P_{ratio} is susceptible to mismatch at and around the resonance frequency ω_r, especially for *LiTeCon-V1*, which does not capture the optimal force-to-velocity response at those frequencies both in magnitude and phase and results in $P_{\text{ratio}} > 1$. Additionally, *LiTeCon-V2* has poor matching characteristics, but the mismatch around resonance is not as poor as *LiTeCon-V1*. Therefore P_{ratio} is always less than 1 for this controller

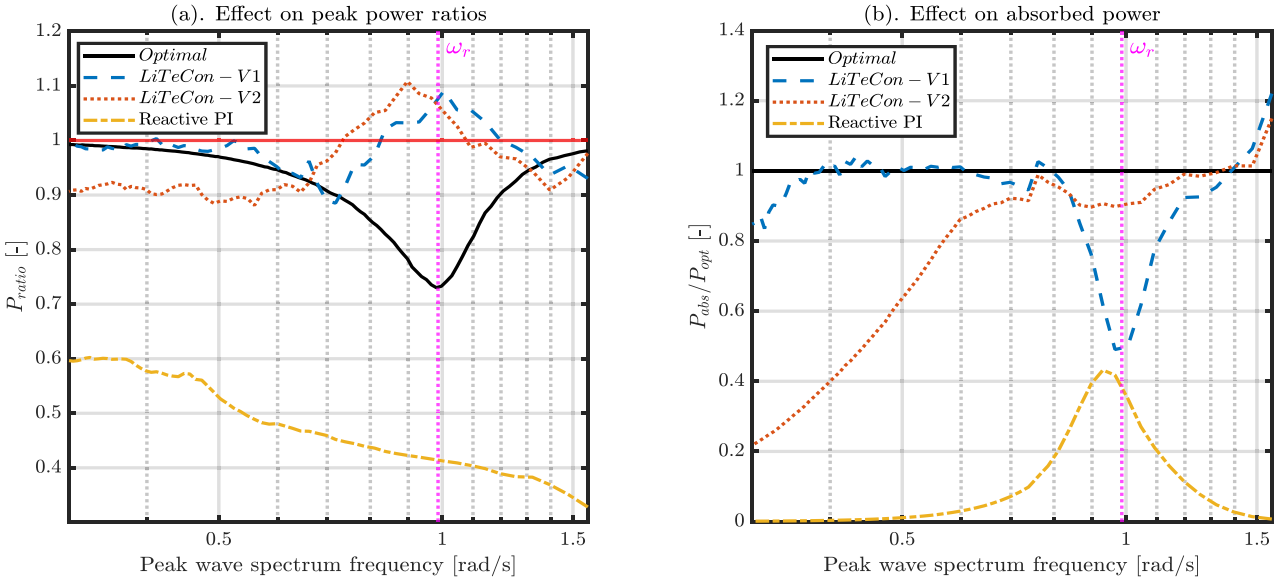

FIGURE 13. Effects of controller synthesis mismatch under panchromatic waves: (a) Peak power ratio P_{ratio} of the controllers for the range of wave frequencies considered. (b) Relative absorbed power P_{abs}/P_{opt} of the controllers for the range of wave frequencies considered. The vertical purple dotted line depicts the resonant frequency ω_r of the WEC.

realisation. Still, it is important to note that the power capture performance of *LiTeCon-V2* is significantly poorer than *LiTeCon-V1*, as shown in Fig. 12(b). On the other hand, the *Reactive PI* realisation can only map a single frequency on the optimal impedance-matching condition and results in the least relative absorbed power P_{abs}/P_{opt} and P_{ratio} values among the considered controller realisations, as depicted in Fig. 12.

For the panchromatic case, the effects of controller mismatch on P_{ratio} are more pronounced, as depicted in Fig. 13. Specifically, Fig. 13(a) shows that the $P_{\text{ratio}} > 1$ for both *LiTeCon-V1* and *LiTeCon-V2*, for mismatches around the resonant frequency (ω_r) of the WEC. Consequently, the negative impact of the increased P_{ratio} on the relative absorbed power P_{abs}/P_{opt} is illustrated in Fig. 13(b), which shows a significant drop in relative absorbed power. The *Reactive PI* controller performance, under panchromatic waves, is similar to the monochromatic case in terms of peak power ratio P_{ratio}. A further drop in the relative absorbed power P_{abs}/P_{opt} is observed for panchromatic waves, due to the bandpass nature of the *Reactive PI* controller.

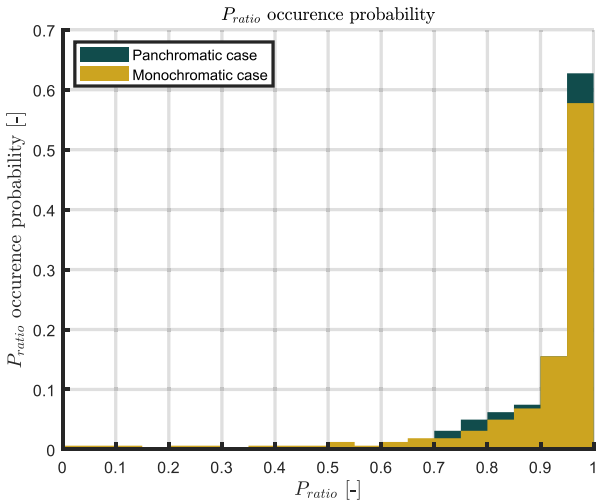

FIGURE 14. Occurrence probability of P_{ratio} values for both monochromatic and panchromatic cases.

VI. DISCUSSION

A. DISCUSSION OF RESULTS

From the results previously discussed in Section V-A, it can be noted that the peak power ratio $P_{\text{ratio}} > 0.7$ for the majority of the matched cases, except for those occurring near WEC resonance frequency. Fig. 14 analyses the data presented in Fig. 6 in terms of probability of P_{ratio} occurrence for both monochromatic and panchromatic ($\gamma = 3.3$) cases and it shows that the reactive power peaks are always in the region of 70-100% ($P_{\text{ratio}} > 0.70$) of the active power peak, for most cases. In addition, the P_{ratio} occurrence probability is the highest (around 70%) when $0.90 < P_{\text{ratio}} < 1$, for both monochromatic and panchromatic cases. Thus, reactive power peaks must be considered of the same magnitude as active power peaks when designing PTO and storage systems.

It is important to highlight that the analytical results, presented in Section IV, provide one critical insight related to the reactive power peaks: the reactive power peaks are *always* less than the active power peaks in a matched system/controller case. Conversely, the **only** situation where large (in excess of active power) reactive power peaks occur is when there is system/controller mismatch, which results in peak power ratios $P_{\text{ratio}} > 1$. Importantly, an increased peak power ratio $P_{\text{ratio}} > 1$ always results in a significant drop in absorbed power, as demonstrated in Section V-B. Higher reactive power

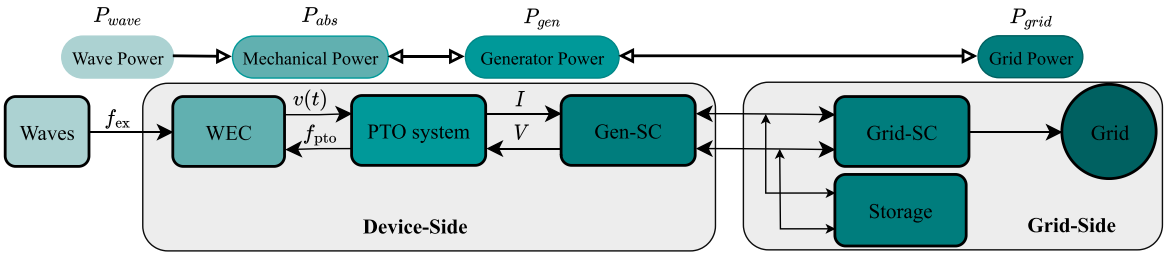

FIGURE 15. A typical wave-to-grid (W2G) wave energy conversion system.

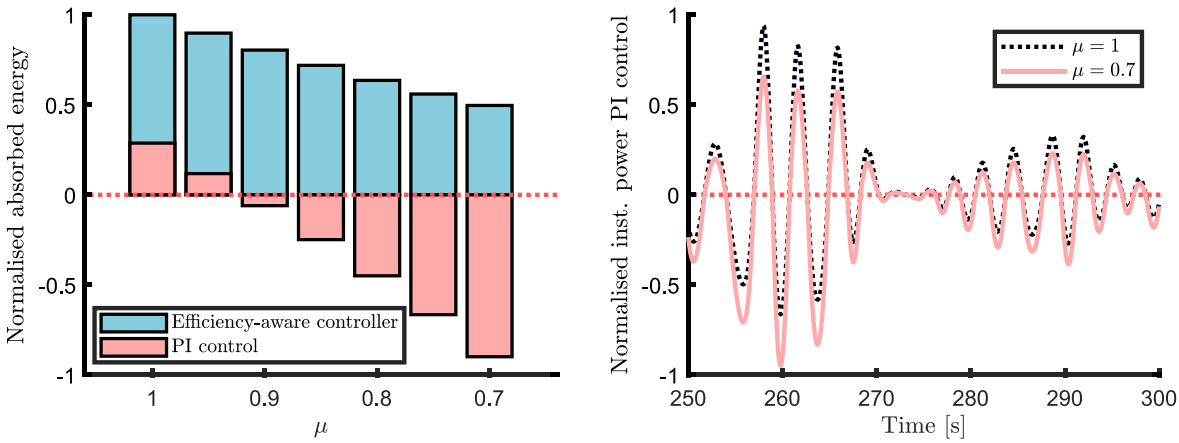

FIGURE 16. Ranges of positive and negative energy absorption for non-ideal PTO case, using an efficiency-aware (moment-based), and efficiency-ignorant (reference) PI controller, using the methodology of [39] (left). Sample time trace of power flow with non-ideal PTO for an efficiency-ignorant (reference) PI controller, showing large excursions in reactive power flow (right).

peaks, indicative of a mismatch, are caused by various reasons (see Section V-B) and can be dealt with in different ways by addressing the mismatch. First, the model used for control design needs to be as good as possible, to remove modelling uncertainties, which in turn prevents extreme reactive power peaks. Alternatively, the use of model-free (data-based) controllers [38] for WECs can be a solution to this problem, but these controllers are at an early development stage (and constraint handling is an issue). Another way to avoid excessive reactive power peaks is to constrain reactive power flow using constrained optimal control approaches, e.g. [18]. However, such a solution involves a nonlinear constraint and cannot guarantee a solution 100% of the time, in addition to being computationally expensive.

The simulation results indicate that the sensitivity of the peak power ratios P_{ratio} to various types of mismatch is different. In particular, P_{ratio} is are more sensitive to the variations in mass M and stiffness K_{h} than of damping B_r variations. Therefore, the worst effects of increased reactive power peaks can be minimised by correctly modelling mass and stiffness parameters. On the other hand, the sensitivity of P_{ratio} to controller mismatch is worst when the controller does not match the optimal impedance-matching condition close to the device resonant frequency, resulting in a drop in the relative absorbed power (see Figs. 12 and 13). To minimise the effects of controller mismatches, the finite order controller realisations need to capture the optimal impedance-matching condition around the device resonant frequency.

It is worth mentioning that the above results are expected to hold for MPC/MPC-like WEC controller cases [7], pursuing the general objective of impedance-matching (complex-conjugate) control. However, the imposition of displacement and force constraints will likely reduce the extent of controller action and, therefore, the peak power ratios.

B. EFFECT OF NON-IDEAL PTO

Our analysis, and sample results, focus primarily on modelling and controller synthesis errors. An important class of modelling error is the non-ideal behaviour in the PTO chain, especially due to non-ideal efficiency in the transfer from mechanical to electrical energy. While the focus, in this paper, is specifically on generic system/controller mismatch issues, PTO efficiency deserves some special attention since often, but not always,[4] the ultimate objective is electricity production, with the generator connected to the mechanical prime mover using a suitable coupling. Fig. 15 depicts a typical wave-to-grid wave energy conversion system, which includes both device-side and grid-side components, delineating different power conversion stages and the directions of power flow. In addition, the transformation from mechanical to electrical

[4]Other potential applications include reverse osmosis, for example

energy involves some energy losses due to various conversion stages (see Fig. 15), and some pertinent evidence regarding the behaviour of reactive power peaks under such circumstances is available, and merits discussion.

As a starting point, the studies by Genest et al. [13], [40] show the significant impact of non-ideal PTO efficiency on generated power, demonstrating that, in some cases, the system becomes an overall power *consumer* when non-ideal PTO efficiency is not considered in the controller model. However, importantly, the issue related to reactive power peaks is exaggerated when considering this non-ideal ($\mu < 1$) PTO efficiency, since *even more* reactive power is required at the electrical stage (from the grid) to provide the required mechanical reactive power to 'maximise' hydrodynamic conversion, in the mismatched case, putting unrealistic demands on the power capacity of generator and back-to-back power converter. This is highlighted in Fig. 16.

Clearly, the results from [13], [40], [39], and [41] (which also utilises an efficiency-aware controller) highlight the need for system/controller mismatch, due to non-ideal PTO efficiency, to be considered in the controller model, especially considering the increased power capacity demands (due to non-ideal grid-WEC efficiency) that reactive power peaks place on the generator/converter power rating.

VII. CONCLUSION

This paper examines, via theoretical results and an illustrative case study, the origins of excessive reactive power peaks in reactive WEC control, using the peak power ratio P_{ratio} as a key metric. It can be concluded that the instances of $P_{\text{ratio}} > 1$ are *purely* due to the WEC model/controller mismatch, which arise due to a number of reasons, including unmodelled dynamics, model uncertainty and inevitable controller synthesis errors arising from finite-order realisations, as well as unmodelled non-ideal PTO efficiency. Consequently, the increased P_{ratio} has potential implications for both capital costs of power-train equipment, i.e., PTO and storage systems, and the power absorption capability of the wave energy conversion system. Moreover, power absorption is adversely affected by the increased P_{ratio} for all the cases presented in this study. The study has taken a fundamental (linear) approach, since such results lay important foundations for future work. Since excessive reactive power peaks result from a mismatched system/controller, it may make sense to limit these to rated (active) power, though the mechanism by which this is effectively achieved, and the implications for power absorption, require further investigation.

REFERENCES

[1] B. Guo and J. V. Ringwood, "A review of wave energy technology from a research and commercial perspective," *IET Renewable Power Gener.*, vol. 15, no. 14, pp. 3065–3090, 2021.

[2] S. Astariz and G. Iglesias, "The economics of wave energy: A review," *Renewable Sustain. Energy Rev.*, vol. 45, pp. 397–408, 2015.

[3] H. A. Said and J. V. Ringwood, "Grid integration aspects of wave energy—Overview and perspectives," *IET Renewable Power Gener.*, vol. 15, pp. 3045–3064, 2021.

[4] J. V. Ringwood, G. Bacelli, and F. Fusco, "Energy-maximizing control of wave-energy converters: The development of control system technology to optimize their operation," *IEEE Control Syst. Mag.*, vol. 34, no. 5, pp. 30–55, Oct. 2014.

[5] U. A. Korde and J. Ringwood, *Hydrodynamic Control of Wave Energy Devices*. Cambridge, U.K.: Cambridge Univ. Press, 2016.

[6] D. García-Violini, N. Faedo, F. Jaramillo-Lopez, and J. V. Ringwood, "Simple controllers for wave energy devices compared," *J. Mar. Sci. Eng.*, vol. 8, no. 10, 2020, Art. no. 793.

[7] N. Faedo, S. Olaya, and J. V. Ringwood, "Optimal control, MPC and MPC-like algorithms for wave energy systems: An overview," *IFAC J. Syst. Control*, vol. 1, pp. 37–56, 2017.

[8] H. A. Said, D. García-Violini, and J. V. Ringwood, "Wave-to-grid (W2G) control of a wave energy converter," *Energy Convers. Manage. : X*, vol. 14, 2022, Art. no. 100190.

[9] J. V. Ringwood, S. Zhan, and N. Faedo, "Empowering wave energy with control technology: Possibilities and pitfalls," *Annu. Rev. Control*, vol. 55, pp. 18–44, 2023.

[10] N. Y. Sergiienko, M. Cocho, B. S. Cazzolato, and A. Pichard, "Effect of a model predictive control on the design of a power take-off system for wave energy converters," *Appl. Ocean Res.*, vol. 115, 2021, Art. no. 102836.

[11] J. K. Shek, D. E. Macpherson, M. A. Mueller, and J. Xiang, "Reaction force control of a linear electrical generator for direct drive wave energy conversion," *IET Renewable Power Gener.*, vol. 1, no. 1, pp. 17–24, 2007.

[12] B. Li, D. E. Macpherson, and J. K. H. Shek, "Direct drive wave energy converter control in irregular waves," in *Proc. IET Conf. Renewable Power Gener.*, 2011, pp. 1–6.

[13] G. Bacelli, R. Genest, and J. V. Ringwood, "Nonlinear control of flap-type wave energy converter with a non-ideal power take-off system," *Annu. Rev. Control*, vol. 40, pp. 116–126, 2015.

[14] A. C. M. O'Sullivan and G. Lightbody, "Co-design of a wave energy converter using constrained predictive control," *Renewable Energy*, vol. 102, pp. 142–156, 2017.

[15] H.-N. Nguyen, "Robust adaptive PI control of wave energy converters with uncertain dynamics," *IFAC J. Syst. Control*, vol. 19, 2022, Art. no. 100183.

[16] Y. Zhang, T. Zeng, and Z. Gao, "Fault diagnosis and fault-tolerant control of energy maximization for wave energy converters," *IEEE Trans. Sustain. Energy*, vol. 13, no. 3, pp. 1771–1778, Jul. 2022.

[17] C. Windt, N. Faedo, M. Penalba, F. Dias, and J. V. Ringwood, "Reactive control of wave energy devices–the modelling paradox," *Appl. Ocean Res.*, vol. 109, 2021, Art. no. 102574.

[18] J. K. Jain, O. Mason, H. A. Said, and J. V. Ringwood, "Limiting reactive power flow peaks in wave energy systems," in *Proc. 14th IFAC Conf. Control Appl. Mar. Syst., Robot. Veh.*, vol. 55, pp. 427–432, 2022.

[19] J. Falnes and A. Kurniawan, *Ocean Waves and Oscillating Systems: Linear Interactions Including Wave-Energy Extraction*, vol. 8. Cambridge, U.K.: Cambridge Univ. Press, 2020.

[20] W. Cummins, "The impulse response function and ship motions. DTIC document," in *Proc. Symp. Sh Theory Inst. für Schiffbau der Univ. Hambg.*, 1962, pp. 25–27.

[21] T. F. Ogilvie, "Recent progress toward the understanding and prediction of ship motions," in *Proc. 5th Symp. Nav. Hydr.*, 1964, pp. 2–5.

[22] D. García-Violini, Y. Peña-Sanchez, N. Faedo, and J. V. Ringwood, "An energy-maximising linear time invariant controller (LiTe-Con) for wave energy devices," *IEEE Trans. Sustain. Energy*, vol. 11, no. 4, pp. 2713–2721, Oct. 2020.

[23] LHEEA, NEMOH-Presentation, "Laboratoire de recherche en hydrodynamique Énergetique et environnement atmospherique," 2017. Accessed: Aug. 1, 2022. [Online]. Available: https://goo.gl/yX8nFu

[24] Y. Peña-Sanchez et al., "Finite-order hydrodynamic approximation by moment-matching (FOAMM) toolbox for wave energy applications," in *Proc. 13th Eur. Wave Tidal Energy Conf. EWTEC*, 2019, pp. 1448-1–1448-9.

[25] T. Pérez and T. Fossen, "Time-vs. frequency-domain identification of parametric radiation force models for marine structures at zero speed," *Model., Identification Control*, vol. 29, no. 1, pp. 1–19, 2008.

[26] J. Falnes, *Ocean Waves and Oscillating Systems: Linear Interactions Including Wave-Energy Extraction*. Cambridge, U.K.: Cambridge Univ. Press, 2002.

[27] P. Nebel, "Maximizing the efficiency of wave-energy plant using complex-conjugate control," *Proc. Inst. Mech. Eng., I: J. Syst. Control Eng.*, vol. 206, no. 4, pp. 225–236, 1992.
[28] N. Faedo, F. Carapellese, E. Pasta, and G. Mattiazzo, "On the principle of impedance-matching for underactuated wave energy harvesting systems," *Appl. Ocean Res.*, vol. 118, 2022, Art. no. 102958.
[29] N. Faedo, Y. Peña-Sanchez, and J. V. Ringwood, "Finite-order hydrodynamic model determination for wave energy applications using moment-matching," *Ocean Eng.*, vol. 163, pp. 251–263, 2018.
[30] J. Scruggs, "On the causal power generation limit for a vibratory energy harvester in broadband stochastic response," *J. Intell. Mater. Syst. Struct.*, vol. 21, no. 13, pp. 1249–1262, 2010.
[31] A. Mérigaud and J. V. Ringwood, "Free-surface time-series generation for wave energy applications," *IEEE J. Ocean. Eng.*, vol. 43, no. 1, pp. 19–35, Jan. 2018.
[32] N. Faedo, G. Giorgi, J. Ringwood, and G. Mattiazzo, "Optimal control of wave energy systems considering nonlinear Froude–Krylov effects: Control-oriented modelling and moment-based control," *Nonlinear Dyn.*, vol. 109, no. 3, pp. 1777–1804, 2022.
[33] R. A. Horn and C. R. Johnson, *Matrix Analysis*. Cambridge, U.K.: Cambridge Univ. Press, 2012.
[34] A. Scavalla, A. Rossi, V. L. Battaglia, and N. P. Belfiore, "A survey of wave energy converter mechanisms presented under the topological and functional viewpoints," *J. Mech. Des.*, vol. 145, no. 7, 2023, Art. no. 070801.
[35] N. Faedo et al., "Energy-maximising experimental control synthesis via impedance-matching for a multi degree-of-freedom wave energy converter," *IFAC-PapersOnLine*, vol. 55, no. 31, pp. 345–350, 2022.
[36] K. Hasselmann et al., "Measurements of wind-wave growth and swell decay during the joint North Sea Wave Project (JONSWAP)," *Deutches Hydrographisches Inst.*, vol. 8, p. 95, 1973.
[37] D. Garcia-Violini and J. V. Ringwood, "Energy maximising robust control for spectral and pseudospectral methods with application to wave energy systems," *Int. J. Control*, vol. 94, no. 4, pp. 1102–1113, 2021.
[38] E. Pasta, F. Carapellese, P. Brandimarte, L. Parrinello, and G. Mattiazzo, "A model-free control strategy based on artificial neural networks for pewec," in *Proc. 14th Eur. Wave Tidal Energy Conf.*, 2021, pp. 1–8.
[39] N. Faedo, G. Giorgi, J. V. Ringwood, and G. Mattiazzo, "Nonlinear moment-based optimal control of wave energy converters with non-ideal power take-off systems," in *Proc. ASME Int. Conf. Offshore Mechanics Arctic Eng.*, 2022, vol. 85932, Art. no. V008T09A082.
[40] R. Genest, F. Bonnefoy, A. H. Clément, and A. Babarit, "Effect of non-ideal power take-off on the energy absorption of a reactively controlled one degree of freedom wave energy converter," *Appl. Ocean Res.*, vol. 48, pp. 236–243, 2014.
[41] N. Y. Sergiienko, G. Bacelli, R. G. Coe, and B. S. Cazzolato, "A comparison of efficiency-aware model-predictive control approaches for wave energy devices," *J. Ocean Eng. Mar. Energy*, pp. 1–13, vol. 8, 2022.

HAFIZ AHSAN SAID (Student Member, IEEE) received the B.Sc. and M.S. degrees in electrical engineering from the University of Engineering and Technology Taxila, Taxila, Pakistan, and the National University of Sciences and Technology, Islamabad, Pakistan, respectively. He has been working toward the Ph.D. degree with the Centre for Ocean Energy Research, Maynooth University, Ireland, since 2019. His research interests include wave energy, control applications, and grid integration aspects of renewable energy sources.

DEMIÁN GARCÍA-VIOLINI received the B.S. degree in automation and control engineering from the National University of Quilmes (UNQ), Bernal, Argentina, in 2010, and the Doctoral degree in engineering from the Buenos Aires Institute of Technology, Buenos Aires, Argentina, in 2015. He is currently a Researcher with the Department of Science and Technology, UNQ, and CONICET, Argentina. He is also with the Centre for Ocean Energy Research, Maynooth University, Ireland. His research interests include control and system ID in wave energy systems, and biomedical engineering. He is currently Guest Editor of IEEE LATIN AMERICA TRANSACTIONS.

NICOLÁS FAEDO was born in Buenos Aires, Argentina, in 1991. He received the degree in automation and control engineering from the National University of Quilmes, Bernal, Argentina, in 2015, and the Ph.D. degree in electronic engineering from the Centre for Ocean Energy Research group, Maynooth University, Kildare, Ireland, in 2020, with a focus on optimal control and model reduction for wave energy converters from a system-theoretic perspective. In 2017, he joined the Centre for Ocean Energy Research group, Maynooth University, Kildare, Ireland. He was a Visiting Researcher multiple times with the Control and Power Group, Imperial College London, London, U.K., in 2018. He holds a postdoctoral position with the Department of Mechanical and Aerospace Engineering, Politecnico di Torino, Turin, Italy. His current research interests include nonlinear optimal control theory and data-driven model reduction, with special emphasis on applications involving renewable energy systems. He was the recipient of a Marie Skłodowska-Curie Actions Individual Fellowship (MSCA-IF 2020), 2022 IFAC CAMS Best Paper Award, 2019 ISOPE Best Student Paper Award and the Exxonmobile Prize, finalist for the 2018 IFAC CAMS Young Author Award, and has been selected as an Outstanding Reviewer two years in a row during 2020–2021, for IEEE TRANSACTIONS ON SUSTAINABLE ENERGY.

JOHN V. RINGWOOD (Senior Member, IEEE) received the Diploma in electrical engineering from the Dublin Institute of Technology, Dublin, Ireland, in 1981, and the Ph.D. degree in control systems from the University of Strathclyde, Glasgow, U.K., in 1985. He is currently a Professor of electronic engineering and the Director of the Centre for Ocean Energy Research at Maynooth University, Ireland. He is also a Chartered Engineer and a Fellow of the Institution of Engineers of Ireland. His research interests include control system design, time series modeling, wave energy, and biomedical engineering. He is on the Editorial boards of the *Journal of Ocean Engineering and Marine Energy*, IEEE TRANSACTIONS ON SUSTAINABLE ENERGY, and *IET Renewable Power Generation*.